UNIVERSIDADE D
COIMBRA

Beatriz Calado Guerra

SINGLE-PIXEL MICROSCOPE FOR BIOLOGICAL SAMPLE ANALYSIS

Dissertation in the context of the Master in Biomedical Engineering, Specialization in Biomedical Instrumentation advised by Prof. João Cardoso and PhD Pedro Vaz and presented to the Faculty of Sciences and Technology / Department of Physics.

July 2023

Faculty of Sciences and Technology
Department of Physics

Single-pixel microscope for biological sample analysis

Dissertation in the context of the Master in Biomedical Engineering
Specialization in Biomedical Instrumentation

Author:
Beatriz Calado Guerra

Supervisors:
Prof. Dr. João Cardoso (LIBPhys)
Dr. Pedro Vaz (LIBPhys)

Coimbra, 2023

This work was developed in collaboration with:

LIBPhys-UC

Acknowledgements

Estando a terminar mais uma fase muito importante na minha vida, quero mostrar a minha gratidão para com todas as pessoas que direta ou indiretamente contribuíram para a realização deste projeto.

Aos meus orientadores, porque foi com muito gosto que desenvolvi este projeto. Ao Dr. Pedro Vaz, pela prontidão e disponibilidade constantes, pela partilha de conhecimento, pela orientação cientifíca e por todo o acompanhamento, preocupação e amizade. Ao Dr. João Cardoso, pelo acompanhamento constante, por me incentivar sempre a superar-me a mim própria e pela oportunidade de desenvolver este trabalho com rigor e perseverança.

À Rute, à Andreia, à Íris e ao Miguel que me acompanharam durante este ano, proporcionando todo o apoio laboratorial e pessoal, em termos de incentivo e entusiasmo para a conclusão deste projeto.

Às minhas amigas Daniela, Diana F. e Diana O. por toda a paciência e incentivo e por todos os momentos de partilha e companheirismo durante estes 5 anos.

Às minhas companheiras de vida Sara, Joana e Sofia, por serem as companheiras de tantas horas em Coimbra, de trabalho e de vida, por me acolherem em suas casas e por me acompanharem sempre nas dificuldades do dia-a-dia. Terão sempre um lugar especial no meu coração!

À minha amiga Ariana, por nunca me ter deixado desistir, por me ter acompanhado em todas as maratonas de tese e por me ter ensinado que a vida é muito mais do que estudar e trabalhar.

Ao meu eterno amigo Miguel, por toda a ajuda e acompanhamento durante este ano. Obrigada por todas as noites de escrita, todas as boleias para o laboratório, toda a disponibilidade para me ajudares no meu projeto, toda a paciência para ouvires as minhas apresentações e sobretudo por todos os dias no laboratório comigo. Sem ti isto não era possível!

Aos meus padrinhos Sónia e Philippe, por me acompanharem sempre com as palavras certas, por me acolherem na melhor cidade que poderia ter escolhido para esta jornada e por me fazerem sempre sentir em casa. E, ao meu avô Pedro, por me incentivar sempre a dar o melhor de mim, por estar presente nesta grande etapa da minha vida e por me ensinar que a vida tem de ser aproveitada ao máximo. Obrigada, por serem a melhor família de Coimbra!

Aos meus afilhados Inês, António, David e Hugo, por serem este orgulho gigante e por confiarem em mim. Obrigada por todo o apoio!

Aos meus companheiros do EMBS IEEE UC e da residência dos Combatentes, por serem uma família e por me apoiarem sempre em todos os desafios e dificuldades.

À minha família: avós, padrinhos, tios e primos por serem o porto seguro a que volto sempre.

À minha irmã Inês, por ser o maior exemplo da minha vida, por me apoiar incondicionalmente em tudo, por ter sempre paciência para mim e por nunca permitir que desista dos meus sonhos. E, ao meu cunhado Daniel, pelo apoio nos últimos 5 anos e por tornar o meu percurso sempre mais tranquilo e bonito.

Aos meus pais Adília e Eduardo, por serem esta força que me mantém sempre firme, por serem o colo e apoio que preciso, por todo o esforço e dedicação durante toda esta jornada e por me terem educado para ser o que sou hoje. É uma sorte gigante ter-vos como pais!

E, por fim, a ti Coimbra, que foste a minha casa durante estes 5 anos e que me viste crescer aproveitando sempre todos os teus recantos e história.

A todos, MUITO OBRIGADA!!

”It always seems impossible until it´s done.”

Nelson Mandela

Abstract

The single-pixel imaging technique allows to reconstruct two-dimensional and three-dimensional images by using a single detector. To obtain this type of image, a single-pixel camera is used. The structure of these cameras is quite simple since it has three main components: a light source, a modulator, and a photodetector. Furthermore, it can be reformulated in different architectures depending on the application where it is used, namely X-ray imaging, fluorescence and phosphorescence imaging, and microscopy, among others.

In the field of microscopy, single-pixel cameras can be built using two types of configuration: structured illumination or selective light detection. In the structured illumination configuration, a projection system is used to illuminate a target, while in selective light detection, a light modulator is used to select only the part of the light that the target has previously reflected or transmitted.

In this work, a prototype of an infinity-corrected microscope based on a single-pixel camera that allows the analysis of several samples was developed. This prototype was built based on the configuration of selective light detection and has in its constitution a Digital Micro-mirror Device (DMD), an acquisition system, and a light detector, which in this case is a photodiode.

Several targets were then tested. The light transmitted by the targets was directed to an objective and a tube lens, which converges the light rays in order to create an image of the target on the DMD. In this device, Hadamard patterns are projected that filter some of the light and reflect it at 12° towards the photodiode. The light arriving at the photodetector was recorded by the acquisition system in order to elaborate the signal processing later. Here, the compressive sensing technique was also tested, using different coefficient percentages for image reconstruction.

The microscope was then characterised using tests that evaluated its optical properties. The system presented a lateral resolution of 44.19 μm on the x-axis and of 62.50 μm on the y-axis. Regarding the field of view, it presented a size of 1.143 mm.

Finally, an application case was made to test the microscope in the imaging field through scattering media. When a scattering media is positioned in front of the object, the results show that a single-pixel camera works better than a traditional pixelated imaging system to reconstruct images of a target of similar quality, regardless of whether or not

the target is obscured by sandblasted glass (the scattering media).

In summary, the values measured for the microscope characterisation satisfy the requirements, the application case was very successful and this prototype has the potential to obtain images with a good resolution and at a much lower cost compared to other techniques.

Keywords: *Single pixel camera, Compressive Sensing, Microscopy, Image reconstruction, Hadamard patterns*

Resumo

A técnica de imagiologia de pixel único permite reconstruir imagens bidimensionais e tridimensionais recorrendo à utilização de um único detetor. Para obter este tipo de imagens, é utilizada uma câmara de pixel único. A estrutura destas câmaras é bastante simples uma vez que, possui três componentes principais entre as quais, uma fonte de luz, um modulador e um fotodetetor. E, pode ser reformulada em diferentes arquiteturas dependendo da aplicação onde é utilizada, nomeadamente imagiologia de raio-x, imagiologia de fluorescência e fosforescência, microscopia, entre outras.

No campo da microscopia, as câmaras de pixel único podem ser construídas utilizando dois tipos de configuração: a iluminação estruturada ou a deteção seletiva da luz. Na configuração de iluminação estruturada é utilizado um sistema de projeção de forma a iluminar um alvo, enquanto que na deteção seletiva da luz, utiliza-se um modulador de luz que seleciona apenas parte desta, que o alvo refletiu ou transmitiu previamente.

Neste trabalho foi desenvolvido um protótipo de um microscópio de correção infinita baseado numa câmara de pixel único que permite analisar diversas amostras. Este protótipo foi construído com base na configuração de deteção seletiva da luz e tem na sua constituição um Dispositivo de Microespelhos Digital (DMD), um sistema de aquisição e um detetor de luz, que neste caso é um fotodíodo.

Foram então testados vários alvos. A luz transmitida pelos alvos foi direcionada a uma objetiva e a uma tube lens, que converge os raios de luz de forma a criar uma imagem do alvo no DMD. Neste dispositivo, são projetados padrões de Hadamard que filtram parte da luz e a refletem a 12° em direção ao fotodíodo. A luz que chega ao fotodetetor é registada pelo sistema de aquisição, a fim de elaborar posteriormente o processamento do sinal. Aqui, foi também testada a aquisição comprimida recorrendo a diferentes percentagens de coeficientes para a reconstrução das imagens.

O microscópio foi então caraterizado com recurso a testes que avaliaram as suas propriedades óticas. O sistema apresentou então uma resolução lateral de 44.19 μm no eixo xx e de 62.50 μm no eixo yy. Em relação ao campo de visão, este apresentou um tamanho de 1.143 mm.

Por fim, foi feito um caso de aplicação de forma a testar o microscópio no campo da imagiologia através de meios de dispersão. Quando um meio de dispersão é posicionado em frente do objeto, os resultados mostram que uma câmara de pixel único funciona melhor

do que um sistema de imagem pixelizada tradicional permitindo reconstruir imagens de um alvo de qualidade semelhante, independentemente do alvo estar ou não obscurecido por vidro areado (o meio de dispersão).

Em suma, os valores medidos para a caraterização do microscópio satisfazem os requisitos, o caso de aplicação teve bastante sucesso e este protótipo tem potencial para a obtenção de imagens com boa resolução e com um custo muito menos elevado comparando com outras técnicas.

Palavras-chave: *Câmara de pixel único, Aquisição Comprimida, Microscopia, Reconstrução de imagem, Padrões de Hadamard*

Contents

List of Figures

List of Tables

List of Abbreviations

2D Two-Dimensional
3D Three-Dimensional

CACSSI Coded Aperture Coherent Scatter Spectral Imaging
CCDs Charge-Coupled Devices
CIS Conventional Imaging System
CMOS Complementary Metal-Oxide-Semiconductors
CS Compressive Sensing

D Image resolution
DAQ Data Acquisition
DAS Digital Acquisition System
DLP Digital Light Processing
DMD Digital Micro-mirror Device
DMDs Digital Micro-mirror Devices

FOV Field of View

He Helium

IR Infrared

LC-SLM Liquid Crystal Spatial Light Modulator

n refractive index
NA Numerical Aperture
Ne Neon
NESTA Nesterov's algorithm

OPA Optical Phased Arrays
OSA Optical Spectrum Analyzer

PD Photodetector
PSF Point Spread Function

SLR Single-Lens Reflex
SNR Signal-to-Noise Ratio
SP-CACSSI Single-Pixel Coded Aperture Coherent Scatter Spectral Imaging
SPC Single-Pixel Camera

SPCs Single-Pixel Cameras
SPI Single-Pixel Imaging
SR Sampling Ratio
SWIR Short-Wave Infrared

TVAL3 Total Variation minimization by Augmented Lagrangian and ALternating direction ALgorithms

USAF United States Air Force
UV Ultraviolet

VGA Video Graphics Array

XRD X-Ray Diffraction

1

Introduction

1.1 Motivation

The persistent desire to overcome obstacles and learn new things are fundamental qualities of humans. As it relates to science, this causes ongoing technical advancement and, as a result, the creation of new tools.

These innovations have improved imaging technology steadily, making it easier to obtain photos with good resolution and quickness. There are always things that may be done better, though, as this field is continually developing. In reality, there is a growing need for more storage space as well as access to parts of the electromagnetic spectrum that are reportedly inaccessible when utilizing conventional cameras.

Nowadays, we have cameras with pixelated array detectors at our disposal. The two common 2D sensors are Complementary Metal-Oxide-Semiconductors (CMOS) and Charge-Coupled Devices (CCDs). The number of sensor components in the detector array is always rising as a result of the ongoing demand for higher image resolutions. Additionally, the Shannon-Nyquist theory [1] dictates the sampling frequency for cameras used in lifetime imaging, which generates a huge amount of data. The sensors employed in lifetime imaging must be able to capture the phosphorescence wavelength of the molecule at extremely fast frame rates. Because 2D sensors are expensive and occasionally even unavailable in specific spectral regions, utilizing them may be challenging.

Using a single-pixel photodetector and the mathematical concepts of the Compressive Sensing (CS) theory is a good solution for this sensors' problem. The spectral band constraint is no longer an issue when employing a unidimensional detector because it is possible to access a broader region at lower costs. Additionally, achieving high frame rates is simpler. By employing a sampling frequency that is lower than that required by the Nyquist theorem, compressive sensing enables the reduction of data collection. In this method, the sample is illuminated by a series of binary light patterns. The photodetector gathers the resultant light, and with the help of a reconstruction algorithm, it is possible to create a 2D image of the sample [2].

The adaptability of this imaging technique is useful in the microscopy field for seeing biological materials at various wavelengths while upholding the fundamental principles and ideas of image collection and reconstruction.

1.2 Goals

The main goal of this thesis was to develop a single-pixel microscope prototype to analyze several samples. For this, it was necessary to improve the Single-Pixel Imaging (SPI) system already available at the LIBPhys in terms of software and hardware.

The new prototype is composed of a light modulator using a Digital Micro-mirror Device (DMD), a Digital Acquisition System (DAS) and a photodiode, mainly. It will be used to study biological samples and in particular, to observe phosphorescent samples containing a molecule sensitive to the oxygen concentration of the medium, at a later stage.

For the microscope assembly, it was necessary to fulfil a set of goals, such as programming the components used (DLP and DAS), calibrating and aligning all the components of the assembly and finally evaluating the characteristics of the microscope, namely the Field of View (FOV) and lateral resolution. With this, it was possible to check whether it would be a good microscope for the observation of biological samples.

1.3 Workflow

Figure 1.1 displays the seven main objectives that were designed for this thesis along with a timeline over the last 11 months.

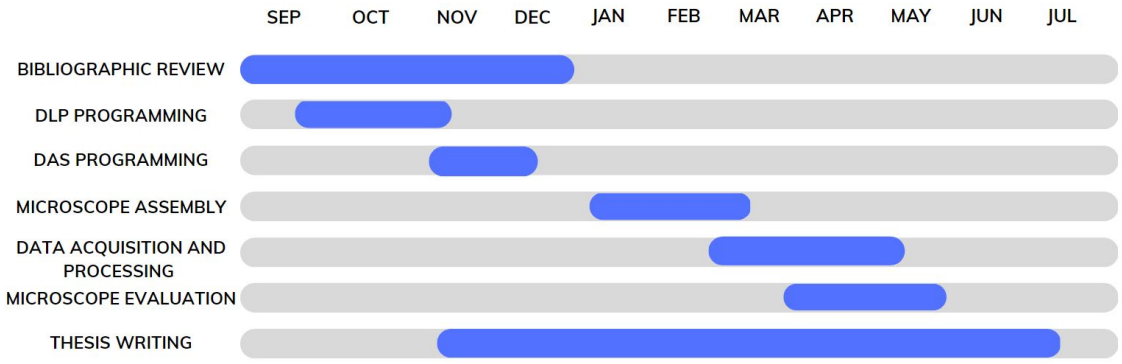

Figure 1.1: Gantt chart of the thesis project.

1.4 Research Team

The development of this master's thesis took place at LIBPhys throughout the 2022–2023 academic year. Instrumentation, biomedical engineering, and radiation physics are the main study areas of the LIBPhys research centre, which is located at the Physics Department of the University of Coimbra.

BSc Beatriz Guerra PhD Pedro Vaz Professor João Cardoso	LIBPhys

1.5 Scientific Contributions

The work developed during this project resulted in the following scientific contribution:

Proceedings - Pedro G. Vaz, Beatriz C. Guerra, and João Cardoso, "Single-pixel imaging: concepts and application to imaging through scattering media.," in Proceedings of the 23^{th} International Conference on Transparent Optical Networks, 2023.

Presentation - Pedro G. Vaz, Beatriz C. Guerra, and João Cardoso, "Single-pixel imaging: concepts and application to imaging through scattering media.," in 23^{th} International Conference on Transparent Optical Networks, 2023. 6 July 2023, Bucharest, Romania.

1.6 Requirements analysis

To start the project with some notions of the expected results, initial requirements were set for the field of view and lateral resolution values on the x-axis and y-axis [3].

Table 1.1: Requirements for FOV and lateral resolution.

Parameter	Value
Field of View (FOV)	$1280\mu m$
Lateral resolution	$< 10\mu m$

1.7 Document Structure

This dissertation is organized into five chapters.

- Chapter 1 - Introduction - This chapter includes the project's primary objectives and motivations, the workflow, the research team that collaborated on it, a list of scientific contributions and the requirements for setting up the single-pixel microscope.
- Chapter 2 - Background - This chapter gives a brief overview of the theory supporting the themes of this dissertation. Firstly, the single-pixel technique is explored as well as the image reconstruction algorithm used. The microscopy field and its relation with single-pixel imaging are also presented here. The state of the art in the fields of SPI and microscopy is also covered in this chapter.
- Chapter 3 - Materials and Methods - The materials and techniques utilized in the various stages of the project development are presented in this chapter. The chapter

begins with a description of the experimental setup, followed by the different steps taken, from the microscope control process to microscope evaluation.

- Chapter 4 - Results and Discussion - The results of the methodology's multiple phases are presented in this chapter. Here, the discussion of the obtained results is also described.
- Chapter 5 - Conclusion - The general conclusions and findings of this work are included in this chapter along with a description of potential future advancements and research directions.

2

Background

2.1 Single-Pixel Imaging (SPI)

SPI is a method of imaging that has recently received a lot of interest from several fields. Using only a single-pixel detector, the SPI method can reconstruct 2D and 3D images [4].

The SPI approach is physically implemented by the Single-Pixel Camera (SPC). A SPC is a device that captures images by probing a scene with a sequence of spatially defined patterns and measuring the corresponding intensity on a detector lacking spatial resolution [5]. A SPC can be built using either structured illumination or selective light detection and it is made up of three primary parts in both configurations: a light source, a spatial light modulator, and a photodetector [6].

2.1.1 Context

The development of the flying-spot camera in the 1920s may have marked the beginning of the application of the SPI method. The Nipkow disc, a pattern with evenly spaced and sized holes, was used in that technology, which was a mechanical scanning imaging system, to convert visual pictures into electrical signals. When two-dimensional imaging sensors weren't available, this system could be used to transform images into electrical signals [7].

After that, this method has undergone scientific and technical advancements that have made it a revolutionary technology that has advantages over conventional imaging methods [7].

Sen *et al.* [8] released the paper "Dual Photography" in 2005, proposing the idea that an image might be acquired using just a single photodetector (single-pixel detector) rather than a detector array as utilized by the majority of common imaging devices, including mobile phones and digital SLR cameras. The single-pixel detector is used to measure the associated intensities while a sequence of spatially defined patterns is used to probe the scene. This provides the spatial structure in this case. Many applications in the visible wavelength spectrum now have access to low-cost, high-performance imaging technologies because of the development of Charge-Coupled Devices (CCDs) and Complementary Metal-Oxide-Semiconductors (CMOS) pixelated sensors. Single-pixel detectors, on the

other hand, might offer important performance advantages like sensitivity at non-visible wavelengths or extremely accurate timing resolution, both of which can be difficult or prohibitively expensive to construct as a pixelated imaging device [9].

After, following the advancement of compressive sensing, Duarte *et al.* [10] at Rice University reported the idea of single-pixel imaging in a seminal publication. This groundbreaking work is a fusion of various imaging and sampling techniques that have influenced the field of single-pixel imaging and established the groundwork for recovering images from a single-pixel camera when the number of measurements is less than the sum of the unknown pixels in the image, that is, when the properties of the image are sensed compressively, also known as sub-sampling [9].

Single-pixel imaging has made cutting-edge detector technologies an ideal testing ground, enabling the creation of affordable imaging systems over a large band of the electromagnetic spectrum [9].

2.1.2 Why SPI?

SPI produces images without the need for a two-dimensional sensor, making use of faster, simpler and more sensitive light detectors that work at wavelengths that are outside the 2D sensor's operating range [7].

When compared to 2D sensors, SPI enables the use of instruments with better signal-to-noise ratios and significantly higher temporal resolutions that operate in spectral regions where pixelated detectors are expensive or nonexistent. Nevertheless, longer acquisition periods and higher digital processing expenses are necessary to rebuild the scene's image from the time-varying intensity measurements, which negates these benefits [6].

The development of quick and dependable light modulators, like Digital Micro-mirror Devices (DMDs) or Optical Phased Arrays (OPA), gave the adoption of SPCs more impact. These devices have great resolutions, and they can change light very quickly (thousands of masks per second). The practicality of the SPC was also aided by the development of image reconstruction techniques that permit compressive sensing, or image reconstruction at a sampling rate significantly lower than the image resolution. These two factors enabled faster and higher resolution SPC, making this technique competitive [6].

2.1.3 Compressive Sensing (CS)

According to the theory, if the two conditions of sparsity and incoherence are met, compressive sensing enables a picture to be reconstructed into an N resolution image by M measurements, where $M < N$ [11, 12]. The ratio between the set of M scene measurements and the N resolution of the recovered image is known as the Sampling Ratio (SR).

When a signal can be represented by high valued coefficients in a certain orthonormal basis (ψ) and the low valued coefficients may be eliminated without suffering large losses, the sparsity criterion is satisfied. This concept is mathematically represented by the discrete signal $x \in \mathbb{R}^{N\times 1}$, whose sparse representation in a particular orthonormal

basis, $\psi \in \mathbb{R}^{N\times N}$, results in high-valued coefficients holding the majority of the spatial information, $\theta \in \mathbb{R}^{N\times 1}$ [13].

$$x = \psi\theta \tag{2.1}$$

The sampling technique used for the signal is related to incoherence. To sample the scene, the sensing matrix (ϕ) needs to have low coherence with ψ. This is accomplished by utilizing a matrix containing independently distributed, identical entries, such as binary entries. The matrix in CS is unaffected by the kind or type of signal that is of interest, leading to a sampling procedure. This can be expressed mathematically as:

$$y = \phi x = \phi\psi\theta = A\theta, \tag{2.2}$$

where $A = \phi\psi$ is an $m \times n$ matrix known as the reconstruction matrix and $y \in \mathbb{R}^{m\times 1}$ is a column vector holding the projections of the sampled data on the sensing basis ($\phi \in \mathbb{R}^{m\times n}$). The matrix representation of the CS encoding equation is shown in figure 2.1.

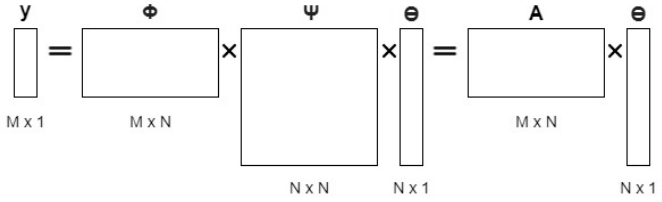

Figure 2.1: CS equations shown as a matrix with the corresponding dimensions [4].

2.1.4 Sensing Basis

The patterns used for structured illumination, or selective detection, must be carefully chosen because CS depends on the collection of a small number of measurements. A strong set of patterns will enable more accurate image reconstruction with fewer samples, cutting down on the time needed to sample the target and the amount of memory required to store both the projection patterns and the sampled data [13].

The impact of pattern selection on image reconstruction quality has recently been the subject of several studies, particularly when the Hadamard matrices are used as the sensing matrices [13] [7]. The Walsh functions build the Hadamard matrix, which is an orthogonal squared matrix that can only hold the two values +1 and -1 [14].

Hadamard matrices' natural order can be calculated using [15]:

$$H_{2^k} = \begin{bmatrix} H_{2^{k-1}} & H_{2^{k-1}} \\ H_{2^{k-1}} & -H_{2^{k-1}} \end{bmatrix} = H_2 \otimes H_{2^{k-1}}, \tag{2.3}$$

with $H_1 = 1$ and 2^k representing the Hadamard matrix's order and the $\otimes$ being the Kronecker product.

In addition to the natural ordering, Hadamard matrices also offer Walsh, Cake-cutting and High-Frequency orderings, among others [13]. The functions in the Walsh ordering are reorganized in a way that their number of zero crossings increases over the lines of the Hadamard matrix. The same information is retained after the reorganization of the lines [15]. In the Cake-cutting configuration, the Hadamard matrix rows are arranged in ascending order of the projected patterns' connected component counts. The definition of a connected component is a continuous collection of pixels with the same value. The Walsh functions were reshaped to the appropriate projection pattern to find Cake-cutting ordering [13]. Related to the High-Frequency ordered Hadamard matrix, this one is created by vertically flipping the Walsh ordered Hadamard matrix [13]. Next, it can be seen the natural order of the Hadamard matrix, in figure 2.2a. Figure 2.2b presents the Hadamard matrix with Walsh organization. In figure 2.2c, one can see the Cake-cutting ordering of 4^{th} order Hadamard matrix. And, figure 2.2d shows the High-Frequency ordering for $k = 4$ of the Hadamard matrix.

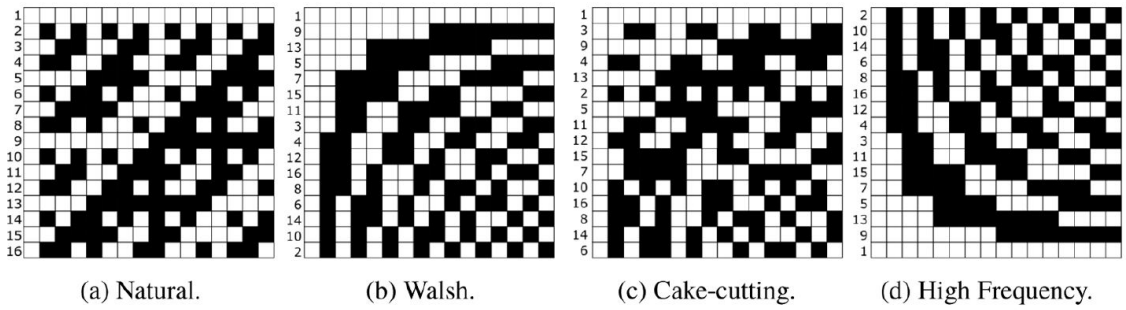

(a) Natural. (b) Walsh. (c) Cake-cutting. (d) High Frequency.

Figure 2.2: Different orderings of Hadamard matrices [13].

2.1.5 Image Reconstruction Algorithm

Even in the setting of compressive sensing, the target image can be rebuilt by the application of the Hadamard inverse transform. This indicates that the reconstruction procedure is quick, simple, and unaffected by any control factors. This procedure can be mathematically described as using a pseudo-inverse sensing matrix [6]:

$$x = (\phi^T \phi)^{-1} \phi^T y. \tag{2.4}$$

There are also more total variation regularization-based image reconstruction techniques, including TVAL3 [16], deep learning (neural networks) [17], and plug-and-play algorithms [18]. These methods outperform a straightforward linear combination of measurements, but they require the solution of lengthy optimization problems or training on big data sets, both of which come with substantial computing costs [6].

2.2 Microscopy

The technical discipline of microscopy involves utilizing microscopes to view objects and materials that cannot be seen without the aid of a magnifying lens. Any method of microscopy in which light is transmitted to the objective lens from a source that is on the opposite side of the sample is referred to as "light microscopy" in general. Typically, a condenser is used to focus the light so that it is as bright as possible on the sample. According to the principle of operation of a microscope, the light enters the sample, passes through the objective lens to enlarge the picture of the sample, and finally travels to the oculars to be viewed [19].

2.2.1 Context

It is unknown certainly who created the first microscope, although, in the early 1600s, Zacharias Janssen, a Dutch sight manufacturer, is credited with creating one of the earliest compound microscopes, those that utilized two lenses. Another Dutchman, Antonie van Leeuwenhoek, created microscopes in the 1660s by hand-grinding his lenses. His basic microscopes, which had just one lens, were more similar to magnifying glasses. With his microscope, on a tiny level, Leeuwenhoek saw fossils, sperm and blood cells, animal and plant tissue, and many other previously unseen items [20, 21].

The production of lenses was hampered by two key issues at the beginning of the 1800s: chromatic and spherical aberrations, which cause colour separation and image blurring, respectively. Joseph Jackson Lister and instrument manufacturer William Tulley created one of the earliest microscopes that addressed both of these issues in 1830. The use of microscopes in science and medicine expanded quickly once these two significant problems were rectified [20, 21].

New tools, such as the electronic microscope, increased the enlargement and provided new perspectives on the body and diseases, enabling scientists to observe organisms like viruses for the first time [20].

Additionally, the use of optical microscopy for micron and sub-micron level examinations across a wide range of fields has grown significantly during the past ten years [22].

Since the construction of the first microscope, the field of microscopy has undergone great advances, making it possible to observe structures never before observed. As this evolution continues, scientists are increasingly seeking to achieve the same quality of microscopic images with less expense and faster acquisition. So now, for example, SPI microscopes are appearing to offer these requirements and many more that are still being discovered.

2.2.2 Microscope Components

The structure of an infinity-corrected optical microscope as it is known, consists mainly of: objective lenses, eyepieces or ocular lenses, a condenser, a tube lens and a light source, as it can be seen in figure 2.3.

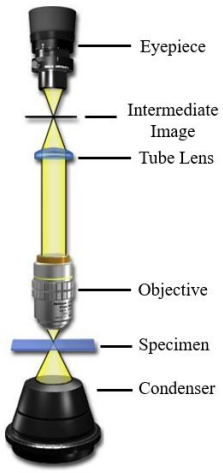

Figure 2.3: Composition of a infinity-corrected optical microscope [23].

To begin with, the multi-element optic closest to the specimen, known as the **objective lens**, is what gathers light from the specimen (or object) first and creates the image that is seen via the eyepiece's focal plane.

In the objective lens, specimens are photographed through a media with a specific refractive index, often air, water, glycerin, or speciality immersion oils, at a very close distance beyond the front focal plane of the objective [22].

Each objective's tube is inscribed with a wealth of knowledge that can be divided into numerous categories (shown in figure 2.4). These include the linear magnification, numerical aperture value, optical corrections, length of the microscope body tube, the kind of media the objective is designed for, and other vital elements that determine whether the objective will function as required [22].

Figure 2.4: Specifications of a microscope objective lens [22].

Eyepieces and microscope objectives work together to further enlarge the intermediate picture so that the specimen's details may be seen. In order to achieve the best results in microscopy, objectives must be used in conjunction with eyepieces that are suitable for the correction and kind of objective. The eyepiece's unique features and purposes are described in inscriptions on its side [22].

In contemporary infinity-corrected systems, the **tube lens** is a multi-element optic that is integrated within and sealed in the observation tube [23]. The distance from the intermediate picture plane grows as the focal length of the tube lens rises, lengthening the tube as a whole. The ideal tube length is thought to be between 200 mm and 250 mm since larger focal lengths will result in a reduced off-axis angle for diagonal light beams, which will lessen system artefacts [24].

In order to illuminate the specimen with parallel beams of uniform intensity from all azimuths over the whole view field, the sub-stage **condenser** collects light from the microscope light source and concentrates it into a cone of light. The sub-stage condenser aperture iris diaphragm must be adjusted every time an objective is changed to provide the correct light cone for the numerical aperture of the new objective [22].

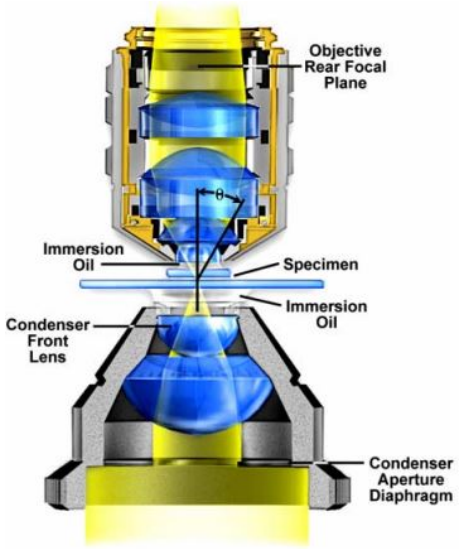

Figure 2.5: Interaction between an objective lens and a condenser in an optical microscope [22].

Figure 2.5 shows a two-lens Abbe condenser. In this image, light from the microscope illumination source enters through the condenser diaphragm at the base of the condenser and is focused by internal lens elements. These elements then project parallel bundles of light into the specimen from each azimuth. By adjusting the aperture diaphragm, the light cone's size and numerical aperture are controlled. The light diverges to an inverted cone with the right angle to fill the front lens of the objective after passing through the specimen.

2.2.3 Microscope Configurations

A microscope can be built using either structured illumination or selective light detection. In structured illumination, a projection system is used to illuminate a target and in selective light detection, a light modulator only chooses a portion of the light the target has either reflected or transmitted. In both situations, the photodiode gathers the scene's elements as well as the mask that the light modulator/projection system has applied [6].

Structured illumination microscopy is a wide-field technique that has been developed to produce better results. This technique involves altering the illumination by superimposing a clear pattern on the sample or its picture. To eliminate the influence of the structure and achieve the necessary performance improvement, computational approaches are applied to the resulting images. Over the previous two decades, this technique has developed as a key illumination approach for optical sectioning, super-resolution imaging, surface profiling, and quantitative phase imaging of microscale objects in cell biology and engineering [25]. In figure 2.6, it is possible to see an example of a structured illumination assembly.

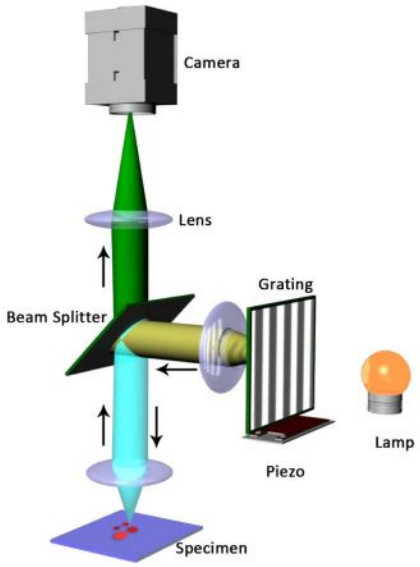

Figure 2.6: Setup for employing structured lighting to achieve optical sectioning [25].

In selective light detection, all the light is projected onto the sample however a light modulator filters out the collected light. That is, part of this light is reflected and part is transmitted. This reflected light is what is captured by the photodetector to be quantified. The final image is reconstructed based only on the light that was reflected on the sample and that reached the photodetector.

2.2.4 Microscope Characteristics

To evaluate a microscope it is necessary to take into account several characteristics such as Field of View (FOV), lateral resolution and Point Spread Function (PSF).

2.2.4.1 Field of View (FOV)

The FOV is the region that the microscope "sees" and it is based on the optics' magnification and the size of the camera chip [26].

In an optical microscope, the diameter of the view field is measured in millimetres at the intermediate image plane and is known as the field number. The field number divided by the objective's magnification provides the field size in the specimen plane [24].

$$Field\ Size = \frac{Field\ Number(f_n)}{Objective\ Magnification(M_o)} \tag{2.5}$$

2.2.4.2 Image resolution

Image resolution (D) is the shortest distance between two points in a specimen that still allows for their separation as distinct objects [26]. The Numerical Aperture (NA) and the wavelength of the light utilized to image the object are the theoretically relevant variables [24].

$$D = \frac{0.61\lambda}{NA} \tag{2.6}$$

The NA is a dimensionless indicator of an optical system's capacity to gather or emit light. It is calculated as the product of the sine of the half angle of the largest cone of light that can enter or depart the lens and the refractive index (n) of the medium. An objective lens's lateral and axial resolution is, respectively, inversely proportional to its NA and NA^2 values [26].

$$NA_{obj} = n \times sin(\theta) \tag{2.7}$$

In real life, other factors like contrast, noise, and sampling also affect the resolution that may be achieved. The axial resolution along the axis of the detecting objective is always worse than the lateral resolution in single-lens microscopy [26].

2.2.4.3 Point Spread Function (PSF)

The Point Spread Function (PSF) represents the appearance of an individual point in the image. When two items A and B are imaged simultaneously in a light microscope, the outcome is equal to the sum of the objects that were imaged separately. Due to this virtue of linearity, it is possible to calculate the picture of any object by splitting it into smaller pieces, imaging each of those, and then adding the results. If these pieces are divided into smaller and smaller pieces, it eventually becomes a collection of point objects that are indefinitely small. Each of these point objects creates a PSF in the image that is scaled and shifted to the associated point's location and intensity, respectively. As a result, the final image is made up of several PSFs. A convolution equation can mathematically describe how an image is created: the object is convolved with the PSF of the imaging

system to produce the acquired image [27].

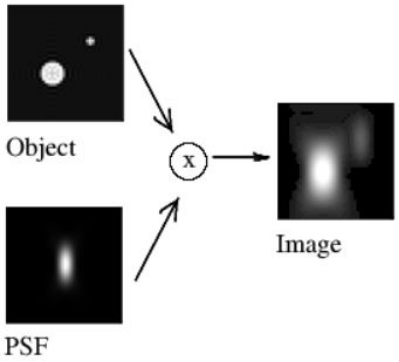

Figure 2.7: Illustration of the Point Spread Function (PSF) [27].

The PSF is a reliable indicator of an optical system's quality since it shows how fuzzy individual points are in an image. The PSF is always normalized, making it simple to compare the PSFs of various systems and, consequently, their imaging capabilities [27].

The type of microscope and the microscopy settings are what determine the PSF's shape. A theoretical PSF can be estimated using model imaging settings if these are known. Deconvolution can then be performed using PSF to increase image quality [27].

2.3 State of the Art

2.3.1 Single-Pixel Imaging (SPI)

Single-Pixel Cameras (SPCs) have been used in multiple areas, over the last decade. Their simple structure and versatility allow them to be reformulated into different architectures for 3D imaging [28], hyperspectral imaging [29], optical computing [30], X-ray imaging [31], phosphorescence and fluorescence imaging [32], microscopy [33], and others [5, 34].

In Sun *et al.* [28], it is possible to see an application of the SPI technique in the field of Three-Dimensional (3D) imaging. In this paper, four single-pixel photodetectors at different locations were used to form a 3D image of an object. It should be noted that each photodetector produced a Two-Dimensional (2D) image. To form this 2D image, a Digital Light Processing (DLP) was used to generate structured illumination. The DLP projected randomly distributed binary patterns directly onto the object, a mannequin head. Then, by rapidly showing 24 binary pictures (bit planes) per frame, Digital Micro-mirror Device (DMD)-based projectors produced colour images. It was possible to demodulate the observed signal at the frequency of the bit plane projection (1440 Hz) by switching between a binary pattern and its inverse in succeeding bit planes. In all iterative approaches, the object's 2D representation was recreated by averaging the ratio between the recorded signal and the incident pattern over a large number of patterns. With this study, they were able

to conclude that using a simple and less expensive system of single-pixel detectors, it is possible to reconstruct high-quality images of real-life objects with a good Signal-to-Noise Ratio (SNR) [28].

Another proposed architecture for SPCs correlates to hyperspectral imaging. In 2012, a high-resolution compressive sensing-based hyperspectral single-pixel imaging system was introduced and demonstrated for the first time. This system incorporated an Optical Spectrum Analyzer (OSA) to provide high spectral resolution acquisition as well as a DMD to optically compress the picture to be acquired. In this paper, a He-Ne laser was used to illuminate the scene and in DMD were projected random binary measurement patterns. In the end, the Nesterov's algorithm (NESTA) was used to reconstruct the images and to demonstrate that the system was able to successfully recreate images with a 10 pm spectral resolution. Another important feature of the system under discussion was its capacity to simultaneously acquire images with excellent spectral resolution from a wide spectral range because it measures all wavelengths simultaneously [29].

In 2014, a compressive imaging technique, that enables snapshot, depth-resolved X-Ray Diffraction (XRD) imaging with a single pixel, was demonstrated. In this study, a spatial code and an energy-sensitive detector were used instead of a time-resolved energy-insensitive detector for spatial-temporal coding. Additionally, a compressive version of Coded Aperture Coherent Scatter Spectral Imaging (CACSSI), which can perform snapshot XRD imaging of a 3D object utilizing a 2D array of energy-sensitive pixels, was able to be realized by employing the ability to code the observed spectrum at the pixel level. Finally, while this method was shown in the context of XRD imaging, SP-CACSSI was capable of being used for single-pixel diffraction imaging at any wavelength. This can be especially helpful at high detector-cost wavelengths like terahertz and gamma rays [31].

Finally, in the field of fluorescence and phosphorescence imaging, it is possible to find some studies related to the SPI technique. For example, in 2021, Santos *et al.* [32] proposed a method in this area. The suggested technique demonstrated an SPC based on structured illumination, that can image phosphorescence in both its lifetime and intensity at the same time. For this, a DLP system was used to project 2D Hadamard patterns of 128×128 pixels, an avalanche photodetector was utilized to capture the sample's light emission and a band pass optical filter was employed to restrict the light to the phosphorescence emission. For image reconstruction, the Total Variation minimization by Augmented Lagrangian and ALternating direction ALgorithms (TVAL3) algorithm was used to restore pictures from a scenario using two similar solutions. It was proved that a basic setup is capable of creating 2D maps of phosphorescence lifetime, opening up new opportunities for applications in the biomedical field in spectral ranges that have not yet been explored or where the instrumentation is expensive [32].

2.3.2 SPI associated with microscopy

Some studies have already been done using SPI in the field of microscopy. Some of the presented SPCs were constructed with selective light detection or structured illumination. A few applications of SPI in microscopy and with different SPC architectures will be presented next.

In an initial approach, in 2012, Grönroos *et al.* [35] demonstrated how an SPC was constructed out of a DLP video projector and a photodiode. To determine which portions of the image should be suppressed and which should be transmitted to the sensor, black and white patterns were fed into the projector. With a refresh rate of 60 frames per second, the patterns were fed through the VGA input, yielding 60 patterns every second. To reconstruct the images, with a resolution of 64×64, the TVAL3 algorithm was used. The developed prototype fell short of expectations since it took up to 60 seconds to sample and recreate a still image. This single-pixel technique is inferior to a conventional camera as a standard visual light camera. However, the method enables the development of a camera that may be sensitive to a wide range of wavelengths of light that is reflected by the DMD, from UV to IR light [35].

In 2014, a study showed a prototype microscope system that uses a single-pixel method to simultaneously image in the visible and Short-Wave Infrared (SWIR). In the paper, a DMD with Hadamard masks with a switching rate of 22 kHz and an objective lens, that provides an image plane with 0.52 Numerical Aperture (NA) and $36\times$ magnification, were used. This optical system was able to perform with a field of view of 381×381 μm, physical resolutions of 12, 6, and 3 μm for mask sizes of 32×32, 64×64, and 128×128, respectively, and frame rates of 10 Hz and 0.6 Hz at 32×32 and 128×128 sizes, respectively. A complete collection of masks was used to create the reconstructions in order to provide the greatest results. The system's SNR affected how well the reconstruction turns out. For the visible and SWIR arms, the resulting SNR of the reconstructed images was 115 dB and 95 dB, respectively. This study demonstrated that the prototype system had a high degree of flexibility, automatically changing from a high frame rate to a high resolution and it proved the compressive technique by just using significant patterns for the reconstruction. The system provided hyperspectrality and significant cost reductions over commercially available systems built on conventional microscopes with IR cameras [33].

Furthermore, in Rodriguez *et al.* [36], a commercial DMD and two single-pixel detectors were attached to an inverted microscope to create a dual-mode optical microscope based on SPI, as it can be seen on figure 2.8. In order to improve resolution and avoid artefacts caused by the so-called diamond pixel architecture, the DMD was used in a configuration of structured illumination. On DLP, Hadamard Patterns were projected with a resolution of 64×64 pixels and a negative USAF test chart (USAF 1951 2×2) was utilised as a sample in the optical setup. Only the two smallest groups from the USAF test—groups, 6 and 7, were used to constrain the system's resolution, reaching a resolution

of 2.76 μm and 2.46 μm in the elements 4 and 5 of group 7, respectively. Additionally, an algorithm was developed to change the geometry of project patterns and for the Compressive Sensing (CS) technique. With the same field of view (192×192 μm) and the same plane, it was shown that the developed system was capable of obtaining images of reflection and transmission modes almost with the same resolution and with a reduction of the 50% of the patterns, exposing structures that were difficult to see with traditional microscopy methods. Due to the employment of specialized sensors, both imaging modes gained from the advantages of SPI such as low-light sensitivity and multidimensional capabilities [36].

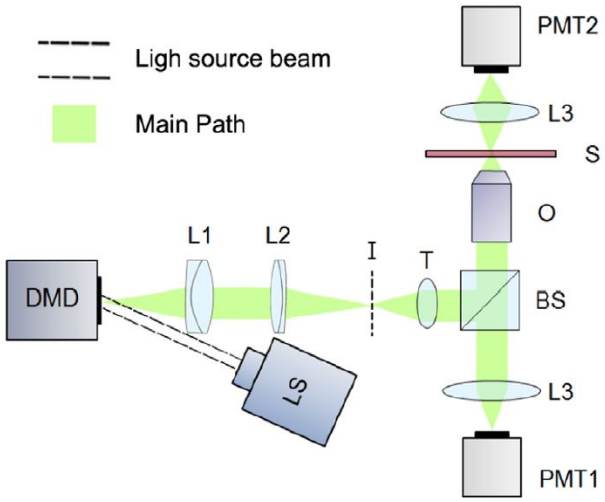

Figure 2.8: Experimental set-up. (LS) Light source. (DMD) Digital micro-mirror device. (L1, L2) Relay lenses. (I) Intermediate image of the DMD. (T) Tubelens. (BS) Beam splitter. (S) Sample plane. (L3) Condenser lenses. (O) Projection objective. (PMT1, PMT2) Reflection and transmission photomultiplier tubes, respectively [36].

Liu *et al.* [37] applied the SPI technique to fluorescence microscopy. This study presented a full-resolution, simultaneous, alignment-free method for fluorescence and phase imaging with single-pixel detectors. In the experimental setup, a DMD, which can refresh binary patterns (Walsh-Hadamard patterns) at a maximum rate of 22.7 kHz, was used. With a frame rate of 20 kHz on DMD and a time of acquisition of 2.5 seconds, the resultant image had a 128×128 pixel resolution. The reconstruction of the images was made by applying the inverse Walsh-Hadamard transform in both phase and fluorescence images. With additional single-pixel detectors or a spectrometer, this technique has a lot of potential for multispectral fluorescence microscopy. Furthermore, this affordable multimodal system may have numerous uses in the field of biomedicine [37]. The interaction field with two arms, the first for phase imaging and the second for fluorescence, is represented in figure 2.9.

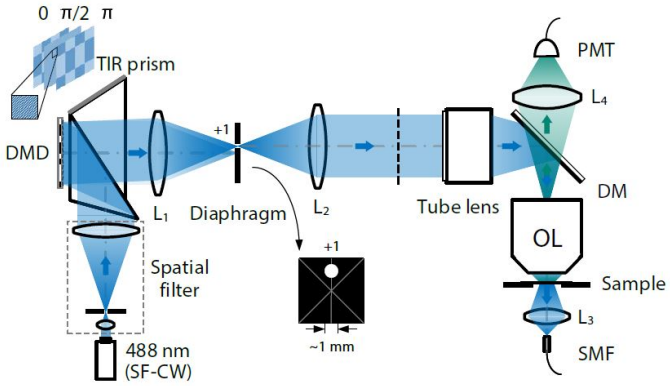

Figure 2.9: Setup for phase and fluorescence imaging experiments using single-pixel detectors. (SF-CW) Single Frequency-Continuous Wave. (DMD) Digital Micromirror Device. (TIR prism) Total Internal Reflection prism. (L1-L4) lenses. (OL) Objective Lens. (DM) Dichroic Mirror. (PMT) Photomultiplier Tube. (SMF) Single-Mode Fiber [37].

In 2020, SPI was suggested as a method for full-colour light-field microscopy so that sampling tasks for the spatial, angular, and colour information could be distributed to both the illumination and detection sides rather than condense on the detection side. For this, were built two experimental setups, the first used a DMD with binary Fourier basis patterns with 384×384 pixels and the second one used a projector to generate colour-coded Fourier basis patterns, that were constructed by multiplying a colour mask with the Fourier basis patterns. The two schemes were reported in this study (figures 2.10 and 2.11) [38].

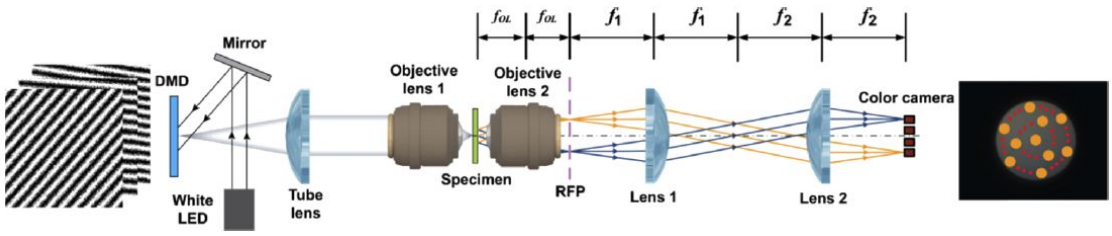

Figure 2.10: Schematic representation of the experimental setup for producing Fourier basis patterns and photographing transmitted samples (RFP: rear focal plane) [38].

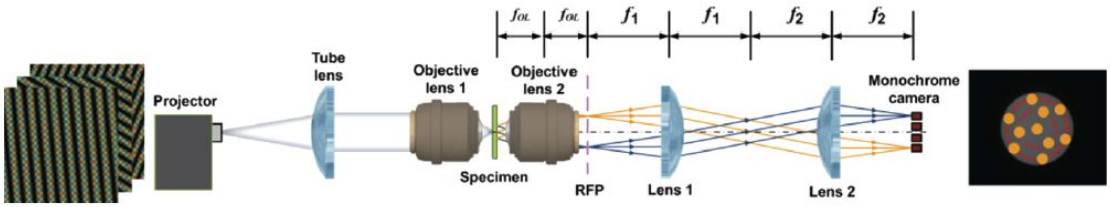

Figure 2.11: Schematic representation of the experimental setup for the production of coloured Fourier basis patterns and imaging of transmitted samples (RFP: rear focal plane) [38].

According to the experimental findings, both systems were capable of reconstructing a full-colour light field without the use of a micro-lens array. In the first scheme, the refocused image had a spatial lateral resolution in the interval: [1.36 μm, 2.72 μm] and in the second assembly, in the interval: [2.72 μm, 5.44 μm]. The second scheme was more effective because it only needs to recover a single image from each single-pixel detector, while the first scheme allowed the reconstruction of a light field with a higher resolution because it was able to record colour information without compromising spatial resolution [38].

Peng *et al.* [39], in 2021, suggested a single-pixel Fourier microscopy method that used structured light to computationally illuminate a sample and a 2D pixelated detector to record the Fourier spectrum picture in the objective's back focal plane. A sequence of time-varying Fourier structured lights was produced using a DMD and an incoherent LED source. Then, as a reconstruction method, the authors of the paper developed the single-pixel algorithm that, allowed the reconstruction of the images from every pixel of 2D pixelated detector by regrouping different pixels of it. The suggested single-pixel Fourier microscopy demonstrated notable improvements in imaging static samples, according to experimental data. As a result, the proposed method might find use in several sectors, such as biology and materials science. In particular, the suggested microscopy will be more suited to characterizing the optical radiation properties of samples in the field of nano-photonics due to the improvement of the imaging function of the standard Fourier microscope [39].

Recently, Deng *et al.* [40] wrote a paper about single-pixel microscopy. Here, the transmissive liquid crystal modulation single-pixel microscope is presented. The suggested microscope's capabilities are calibrated and given a demonstration of the object's multi-spectral microscopic imaging. This study used a LC-SLM to display 15 sinusoidal patterns (128×128). The LC-SLM utilized a frequency of 10 Hz to generate the patterns but the DAQ acquired the signal with 1 kHz, so each image is sampled 100 times. To characterize the microscope a USAF-1951 target was used. Later on in the study, an analysis of the transmissive image of the item behind the scattering material was done. When the scattering medium was positioned between the target and the PD, the microscope performed better. However, the quality of the image dramatically declined when scattering media was positioned between the target and the objective. This may be because the final reconstructed image was decided by how blurry the original pattern was. In any case, compared to the research on the reflective single-pixel microscope, this was the first attempt at a single-pixel microscope using the transmissive optical principle in scattering media imaging. The transmissive single-pixel microscope prototype that has been presented is intended for use in medical imaging and microscopic imaging through scattering media. This paper used the next scheme for the assembly of the microscope (figure 2.12) [40].

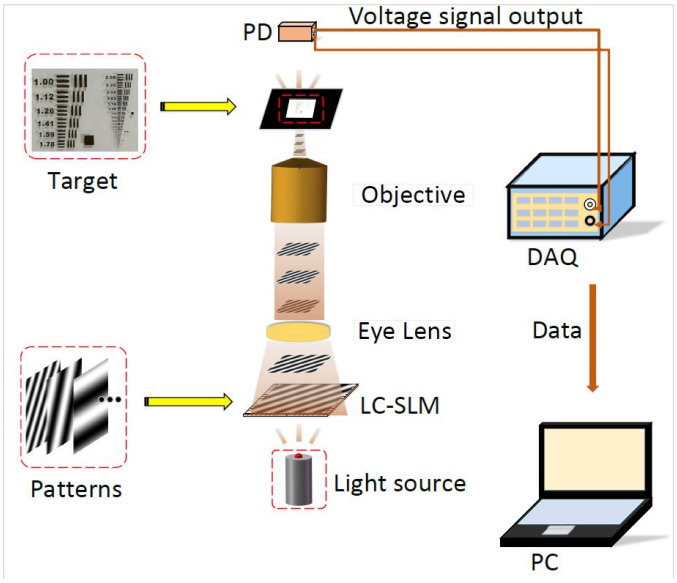

Figure 2.12: Transmissive single-pixel microscopic imaging experimentation principle [40].

3

Materials and Methods

In this project, a single-pixel infinity-corrected microscope, based on selective light detection, was developed to obtain intensity images. The three primary components of the planned SPC were a photodiode to gather the light, a Digital Light Processing (DLP) device to project the patterns to filter the light coming from the sample, and a Digital Acquisition System (DAS) to record the measurements. After this, the Hadamard inverse transform reconstruction algorithm used these measurements to build up the scene's visuals.

3.1 Architecture of the Single-Pixel Camera (SPC)

The experimental set-up included a digital light processing device (DLP LightCrafter^{TM} 4500 - Texas Instruments [41]), a DAS (Analog Discovery 2 - Digilent [42]), a photodiode, a tube lens, an objective lens, a light source (LED 12V) and a lens. The schematic representation of these instruments and their connections is presented in figure 3.1.

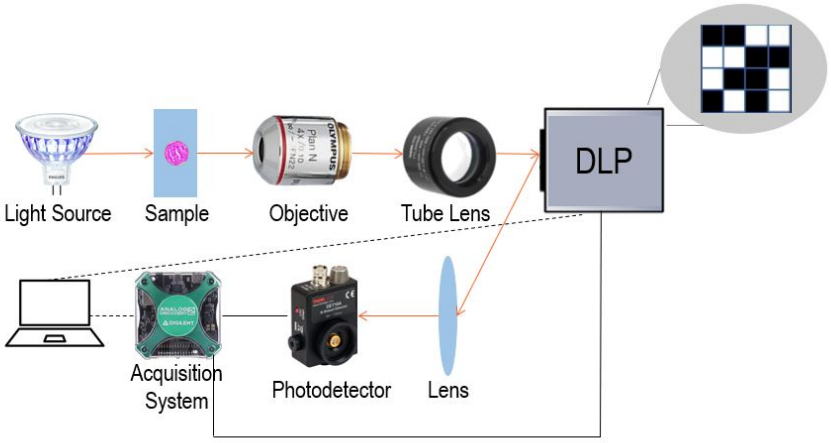

Figure 3.1: Schematic representation of the instruments used for the assembly of the SPC and their connections. The orange arrows represent the passage of light, the black line represents an electrical connection, and the dashed line represents a USB connection.

Firstly, the light is emitted by the light source, goes directly to the target and subse-

quently goes through an objective lens that magnifies the target. In turn, the light coming from the objective lens is directed to a tube lens that transmits the light to the DMD. When the light reaches the DMD, it is reflected at a 12° angle to a convergent lens that captures the reflected light, focusing it on the photodiode. This equipment is directly connected to the acquisition system that contains an integrator and an ADC, thus allowing to store the collected data in a storage device (a computer, for example). In figure 3.2, an optical diagram is presented to explain how the assembled SPC worked.

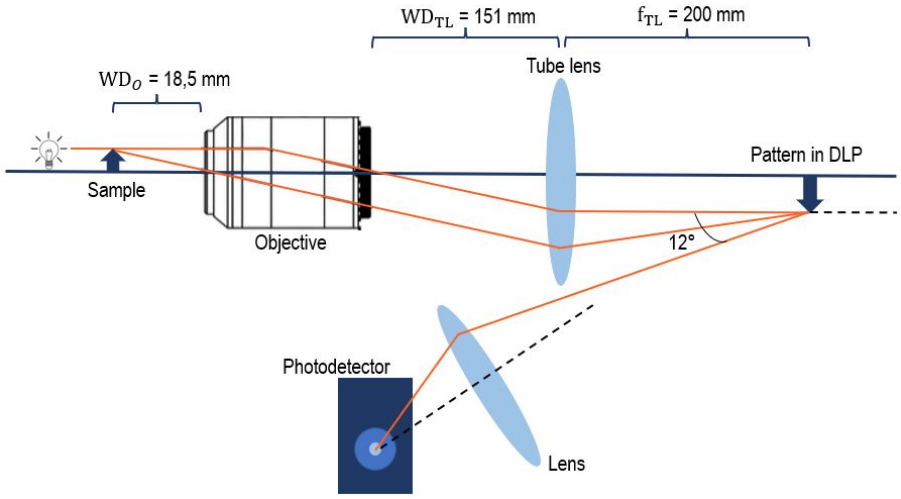

Figure 3.2: Optical diagram of the SPC assembly.

The patterns that the sensing matrix generated were shown by the DLP. The sensing matrix's rows were reconfigured into 128×128 2D patterns. These matrices match Walsh functions chosen from a Hadamard matrix with an order of 14. All these projection patterns were enlarged to a digital image of 512×1024 pixels to fully use the DLP projection area. The DLP mirror configuration causes this image to be projected as a square pattern. The DMD simply displays the numbers 0 and 1, which represent the states OFF and ON, and consequently, the positions of the micromirrors -12 and +12 degrees, in relation with DLP normal vector. The Signal-to-Noise Ratio (SNR) was improved by performing two projections (positive and negative) by each row of the sensing matrix. As a result, the final coefficient value of a particular pattern was equal to the difference between a positive pattern (y_+) and a negative pattern (y_-) as measured by a photodiode:

$$y_p = y_+ - y_-. \tag{3.1}$$

After that, the DAS digitalized the photodiode measurement results. However, this process will be explained in more detail in section 3.2.

The next subsections specify and describe each of the elements used in the assembly.

3.1.1 Digital Light Processing (DLP)

The DLP was one of the most important components of the elaborated assembly. In this case, it is a component from Texas Instruments: DLP LightCrafter 4500 EVM [41]. This device consists mostly of a 912×1140 resolution DMD and a control board containing the DLPC350 DMD controller. For this assembly, the DLP had undergone some modifications as can be seen in the figures 3.3 and 3.4.

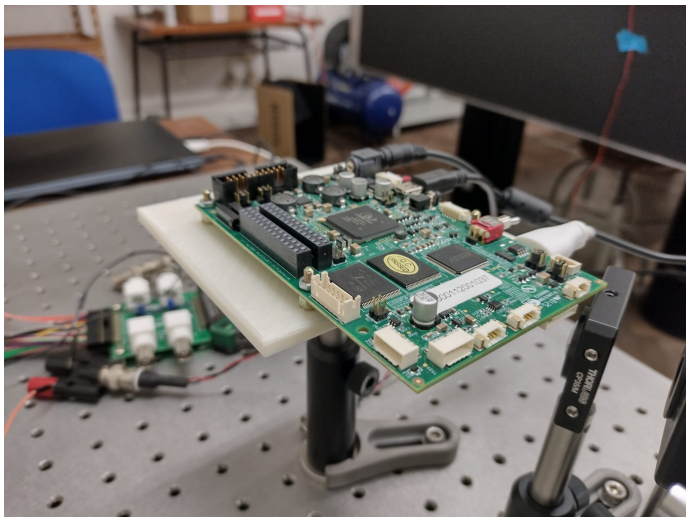

Figure 3.3: DLP viewed from above.

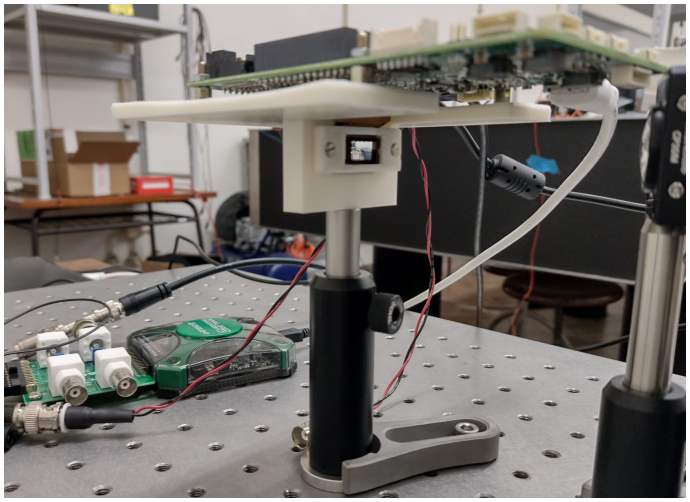

Figure 3.4: DLP viewed from the side.

In the next table (table 3.1), it can be seen some characteristics related to the DLP.

Table 3.1: Characteristics of DLP.

Components	**Characteristics**
Mirror array	Dimensions: 912×1140 | Diagonal: 11.43 mm
Micromirrors	Diamond geometry | Diagonal: 7.6 μm each one
Angle of the mirrors relative to the horizontal position	$\pm 12°$
Rate of patterns change	4 kHz (binary) or 120 Hz (8 bit)
Crossover time of micromirrors	5 μs
Operates for wavelengths	[420; 700] nm

3.1.2 Photodetector

In the experimental setup, the Thorlabs PDA36A2 photodetector [43] was used. This photodiode is very sensitive to low light and integrates a circuit of amplification and the detector. This device is represented in figure 3.5.

Figure 3.5: Picture of the photodetector[43]

In the next table (table 3.2), some characteristics related to the photodetector can be seen.

Table 3.2: Characteristics of the photodetector.

Characteristics	**Values**
Spectral response	[350; 1100] nm
Bandwidth	12 MHz
Diameter of the active area	13 mm
Responsivity	$0.6 \times 10^7 V/W$

3.1.3 Tube Lens

The tube lens used in the SPI microscope assembly was the Thorlabs TTL200-S8 with a design wavelength range between 400 and 2000 nm, an effective focal length of 200 mm, a maximum entrance pupil diameter of 20 mm and a working distance of 151.8 mm. This item can be seen in figure 3.6.

Figure 3.6: Picture of the tube lens.

3.1.4 Objective Lens

In the SPI microscope assembly, the Olympus PLN 4X Objective was used with a numerical aperture of 10, a magnification of 4×, a working distance of 18.5 mm, a field of view of 5.5 mm and a field number of 22 [44].

Figure 3.7: Picture of the objective.

3.1.5 Acquisition System

In the project, an Analog Discovery 2 - Digilent (figure 3.8) was used as DAS. This device was electrically connected to the DLP to detect the trigger signal and, it was connected to the photodetector to acquire the signal it detects, and it was also connected by USB to the computer to save the data collected.

Figure 3.8: Image of the Analog Discovery 2 - Digilent [42].

The ADC resolution is 14 bits and only a channel is used to acquire the signal photodiode so the sampling frequency is 100 Msps, the maximum frequency. However, in the tests performed the frequency used was 1 MHz. The input range is 5 V [42].

3.1.6 Lens

In order to focus the light coming from the DMD onto the photodiode, a positive lens with a focal length of 25 mm was used. As the focal length of the lens is small, the photodiode had to be located very close to the lens so that the light was as focused as possible (for details see figure 4.1 in chapter 4).

3.2 Microscope control process

A Python 3.7 program was created to manage the complete measurement acquisition and storing process. This program allows to configure the DLP variables, namely the exposure time for each pattern. In addition, it allows the initialization of the DLP and the loading of the patterns for subsequent emission. After the emission of all the desired patterns, the photodiode data is recorded by the DAS and stored in the computer memory for subsequent processing.

The next scheme (figure 3.9) represents the developed Python code to control the DLP and the DAS instruments.

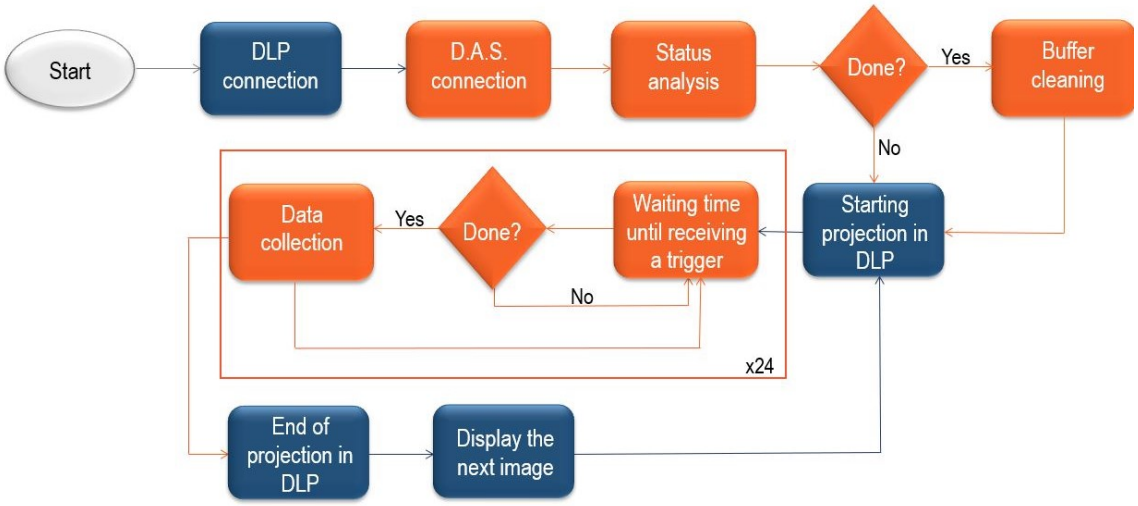

Figure 3.9: Schematic representation of the program used for controlling the single-pixel camera prototype. The blue steps represent the programming part of the DLP, and the orange steps represent the DAS programming part.

Explaining in a general way how the code works, at the first step the connection to the DLP and the connection to the DAS must be established. Next, the state of the DAS was analyzed. If the DAS contained any triggers it had to be cleared, if it did not have any triggers the projections on the DMD could begin. After starting the projection on the DMD, DAS was waiting for some trigger to be received and when it finally received the trigger, it acquired the data from the photodetector. This cycle was repeated 24 times since 24 patterns were stored onto a single image. After the 24 projections, the projection of the first image ended and the next image was projected, restarting the cycle. The code stopped only after all desired images in that acquisition were projected.

3.2.1 Generation of the projection images

The patterns used in the projections in the DLP underwent an adjustment process until they arrived at the final patterns projected in the DLP. The process started with the creation of a Walsh matrix of order 14 (k=14) which gave rise through its rows to 16384 Hadamard patterns with a dimension of 128 $\times$ 128 pixels. After forming these square patterns it was necessary to adjust them to the DLP. Since the DLP's micro-mirrors are diamond-shaped, it was necessary to double the number of rows and expand it to the DLP resolution while keeping only 128$\times$128 pattern zones (forming a matrix of 256$\times$128 pixels). To better understand the process, in figure 3.10, it is possible to see the transformation of the rows of a Walsh matrix of order 4 (k=4) into Hadamard patterns of 4 $\times$ 4 pixels.

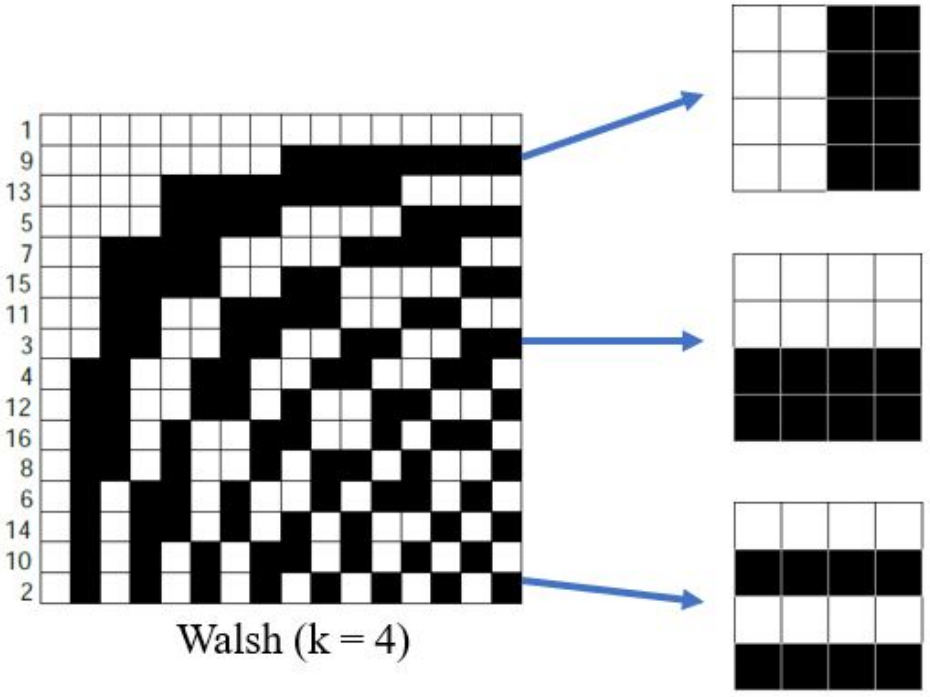

Figure 3.10: Schematic representation of the construction of the Hadamard patterns used [13].

An HDMI cable was used to send the patterns, generated through a code in MATLAB®, to the DMD. This, in turn, was configured to act as a second computer screen, thus allowing it to project any image that the computer screen can display. The DLP's mode of operation allows binary patterns to be output, however, communication via HDMI implies that the images sent must be 24-bit. Therefore, it was necessary to agglomerate 24 patterns, i.e. 24 rows of the sensing Walsh matrix into a single image. This image was then transmitted via HDMI to the DLP which is configured to output each of the binary planes (8R 8G 8B) sequentially. This is an advantage of using this model since it allows to optimize the time needed to perform the emission of the patterns.

Once we had the patterns generated, through a Python code the DLP was configured, the slideshow for sampling the images with the patterns was initialized, and the sampling of the first image started. This process is described in the scheme of figure 3.11.

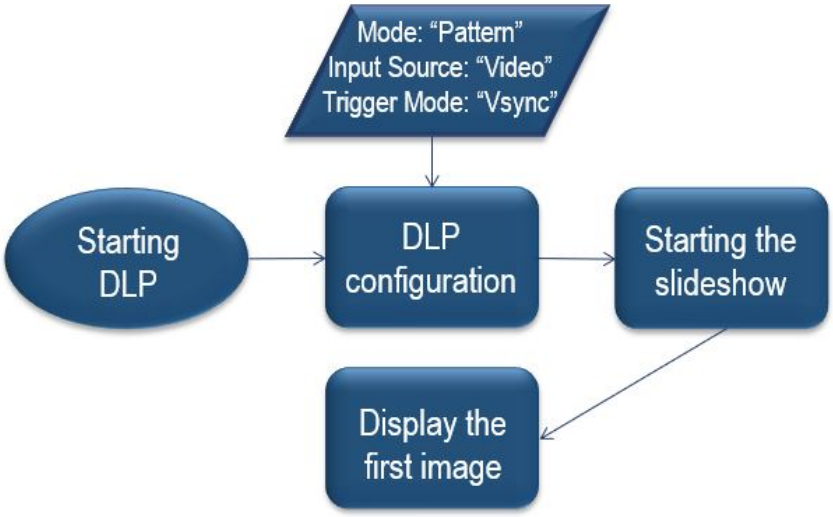

Figure 3.11: Schematic representation of the first programming phase.

3.2.2 Acquisition process

To acquire the data from the photodetector it was necessary to use an acquisition system (Analog Discovery 2 - Digilent) that had to be programmed and configured in a Python code. In figure 3.12, it can be seen the scheme of the elaborated programming code.

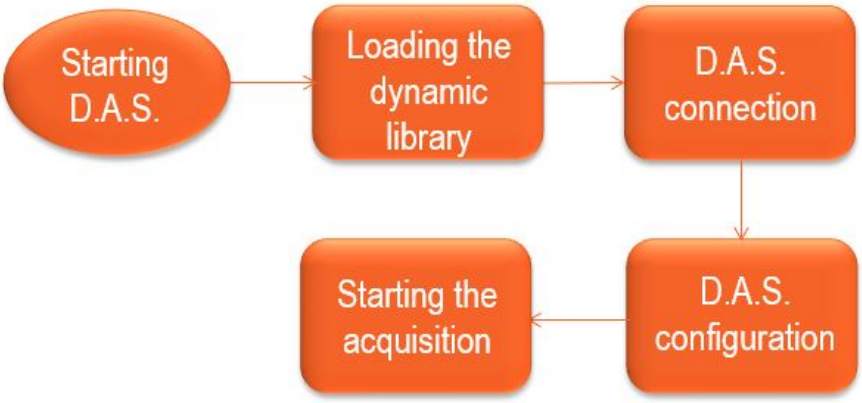

Figure 3.12: Schematic representation of the second programming phase.

In each acquisition, the following parameters were used:

- Number of images = 1366;
- Exposure time = 100 ms / pattern;
- Acquisition frequency = 1 MHz;
- Input range = 5V;
- Number of points acquired per pattern = 128;

To capture the desired image it was necessary to perform several steps that are evident

in figure 3.13.

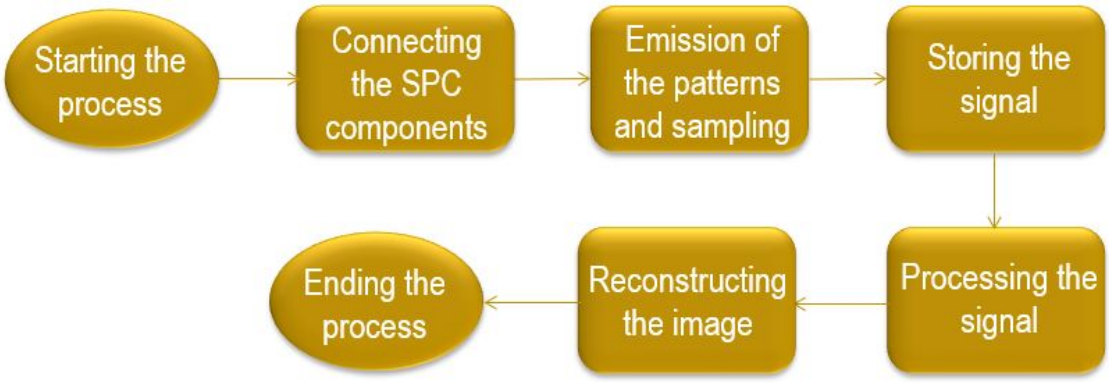

Figure 3.13: Schematic representation of the process to obtain an image from the SPC.

Note that, before starting this whole process, it was necessary to prepare the SPC. That is, adjust the position of the photodiode and the target as well as manually adjust the focus by moving the target to the focal point of the lens. Eventually, these procedures may introduce some errors in the measurements.

3.2.3 Sampling

After all the necessary conditions were met, the sampling process could begin. This step was performed so that it was possible to take several samples for each pattern. This oversampling was required since the signal was uncertain, due to noise, during the period in which the patterns are projected. The total number of patterns used equals twice the number of pixels in the reconstructed image since both normal patterns (called positive) and their negatives were used. This is because according to the study developed by Zhang *et al.* [45], this differential approach allows for the reduction of measurement noise. Thus, in the case where one intends to reconstruct an image with 128×128 resolution, the total number of patterns emitted is $2 \times 16384 = 32784$.

3.2.4 Signal Processing

After the sampling step, the acquired data were processed in a MATLAB® program. From this data, two data files corresponding to the photodiode values for positive and negative patterns were obtained separately.

In order to assign a coefficient to each pattern, the average of the samples was determined for both the positive data file and the negative data file. Next, the negative coefficients were subtracted from the positive coefficients, thus arriving at the final coefficients used later in the reconstruction of the images.

All light sources external to the system have been minimized as much as possible. For this purpose, all measurements were made in a dark room to isolate the assembly from the most varied light interference.

3.3 Microscope evaluation

After the microscope assembly, the evaluation of the developed system's performance is crucial. The optical characteristics of the field of view and lateral resolution were evaluated to determine whether the microscope suited the initial requirements.

The positive 1951 USAF resolution test target from Thorlabs (Thorlabs GmbH, Munich, Germany) (figure 3.14) was used to measure these parameters. This test target consists of various groups of element bars with known dimensions. Each group consists of six elements, and each element is made up of three identically sized horizontal and vertical bars. The smaller the bars are, the higher the group number. The groups go under this as well. The bars' widths range from 0.55 μm to 2000 μm [46].

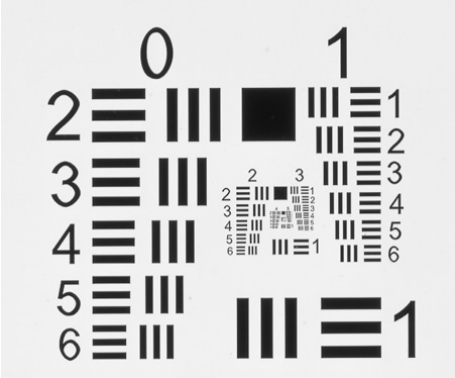

Figure 3.14: Representation of the USAF 1951 target [47].

3.3.1 Lateral resolution

Firstly, the theoretical lateral resolution was calculated using the following formula:

$$D = \frac{0.61\lambda}{NA}. \tag{3.2}$$

where λ is the wavelength and NA is the numerical aperture of the detection objective [24].

The wavelength used was 550 nm and the NA of the objective used was 0.10. Therefore, it can be concluded that the theoretical lateral resolution was:

$$D = \frac{0.61 \times 550}{0.10} = 3.36\mu m. \tag{3.3}$$

Then, the lateral resolution was measured experimentally. For this, the Rayleigh criterion had to be taken into consideration. The Rayleigh criterion states that the contrast between the Point Spread Function (PSF) and the valley between the two adjacent peaks is 26.4% when the condition of minimal separation is met. The lateral resolution is determined by the relative amplitude of the peak and valley intensities [48].

A MATLAB® code was built to average the pixels of the dark zones (vertical and

horizontal bars of the USAF 1951 target) and the adjacent light zones between the bars, to create a more realistic plot of the peaks and valleys of each element of each group acquired. From this plot, it was possible to determine the minimum value (smallest value among the three bars), the valley and the maximum value (value of the light zone underlying the minimum), the peak, and, in order to calculate the contrast value, to subtract the maximum value minus the minimum value.

Once the elements of the groups with a contrast closest to 26.4 % were known, it was possible to determine the lateral resolutions on the x-axis and y-axis through the size of the bars of the chosen elements.

3.3.2 Field of View (FOV)

As in the lateral resolution subsection, the theoretical value of the FOV was calculated. For this, it was necessary to calculate the effective magnification (M_0) of the system with the following expression:

$$Effective\ M_0 = Design\ M_0 \times \frac{f_{Microscope\ tube\ tens}}{f_{Design\ tube\ lens}} = 4 \times \frac{200mm}{180mm} = 4.44. \tag{3.4}$$

From the value of the effective M_0, it was then possible to calculate the field size from the formula 3.5.

$$Field\ Size = \frac{Field\ Number(f_n)}{Objective\ Magnification(M_o)} = \frac{22}{4.44} = 4.95mm. \tag{3.5}$$

After knowing the field size, it was necessary to know what percentage the active area of DMD occupied of this total field (viewing percentage)(equation 3.6) and the size of the final image on the DMD, the FOV (equation 3.7).

$$Viewing\ percentage = \frac{DMD\ width}{Field\ Number(f_n)} \times 100\% = \frac{6.616}{22} \times 100\% = 30.7\%. \tag{3.6}$$

$$FOV = Viewing\ percentage \times Field\ Size = 30{,}7\% \times 4.95 = 1.49mm. \tag{3.7}$$

After the theoretical calculations, the FOV determination was carried out experimentally. It was needed to know how many pixels were equivalent to the size of every picked bar, which was known because of the test target requirements. The image on DMD contained 128×128 pixels, as it was already known. Given this, figuring out the FOV was simple. For larger bars, it was simpler and more reliable to determine the FOV value.

To facilitate the counting and determination of the FOV, the number of pixels from the start point of the first bar to the end point of the last of the three bars was counted for

both the x-axis and the y-axis. A simple rule of three was then worked out between the number of pixels counted and the combined size of the bars and the clear zones between the bars, to arrive at the final FOV value.

3.3.3 Amplification

From the FOV value, it was possible to calculate the amplification value of the single-pixel microscope from the following expression:

$$Theoretical\ amplification = \frac{DMD\ width}{FOV} = \frac{6.616}{1.49} = 4.44. \tag{3.8}$$

This value corroborates the value of the effective magnification (M_0). Then, the amplification was calculated with the same expression but with the experimental FOV value.

3.4 Application Case

3.4.1 Imaging through scattering media

In order to test the microscope, simulation work and an experimental setup were made to show the capabilities of SPI to obtain images through scattering media [6].

The experimental configuration was modified to demonstrate an SPC's ability to picture a target through a scattering medium. A positive 1951 USAF resolution test chart, a single pixel microscope, an LED light source, and a sandblasted glass (Edmund optics #43-724) put between the photodetector and the light modulator composed this setup. Figure 3.15 shows the diagram of this setup.

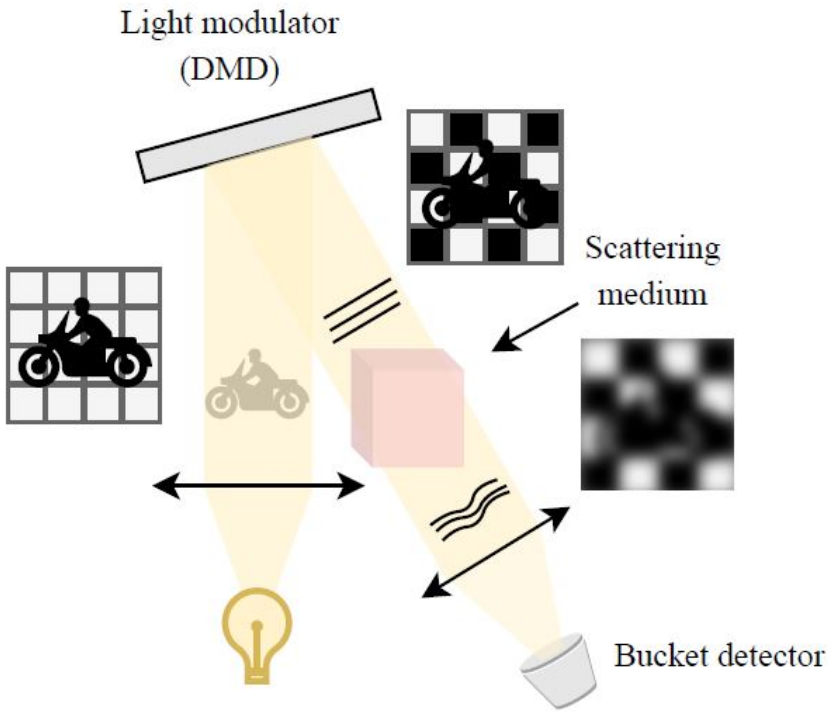

Figure 3.15: Diagram of the simulated set-up [6].

Finally, the USAF group 2, element 5, came into focus under the microscope. Image acquisition was then performed with a frequency of 1 MHz, an exposure time of 80 ms and 128 points per pattern [6].

4

Results and Discussion

4.1 Architecture of the Single-Pixel Camera (SPC)

In this section, the final assembly of the single-pixel microscope will be presented, with all the materials used and the final configuration.

4.1.1 Microscope Assembly

In the next pictures, the assembly performed in the laboratory can be seen, from above (figure 4.1) and from the side view (figure 4.2). Each number in the pictures represents a component. The number 1 represents the light source, the target is represented by the number 2, the 3 symbolizes the objective lens, the tube lens is represented by the number 4, the 5 indicates the DLP, the positive lens is symbolized by the 6, the number 7 demonstrates the photodiode and finally, the number 8 represents the DAS.

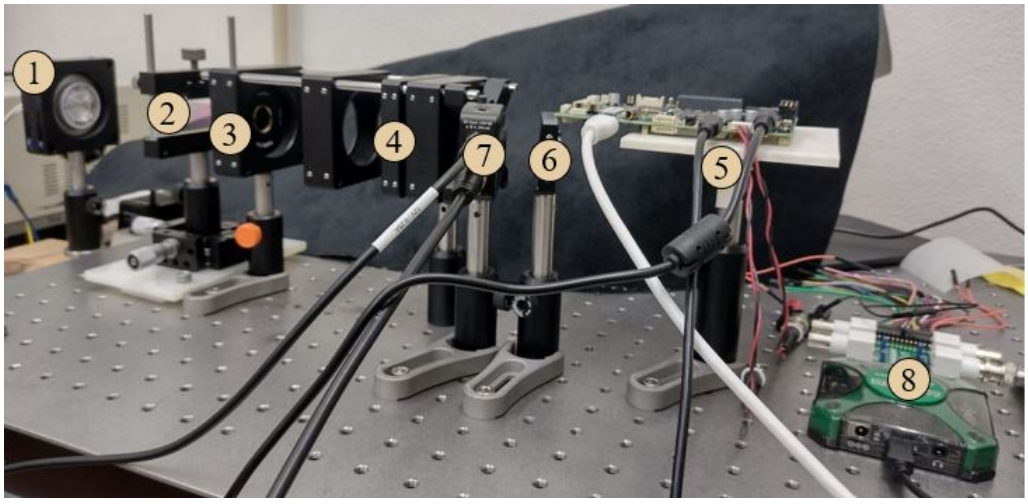

Figure 4.1: Assembly of the SPC seen from the side. 1- Light Source; 2- Target; 3- Objective lens; 4- Tube lens; 5- DLP; 6- Positive lens; 7- Photodiode; 8- DAS.

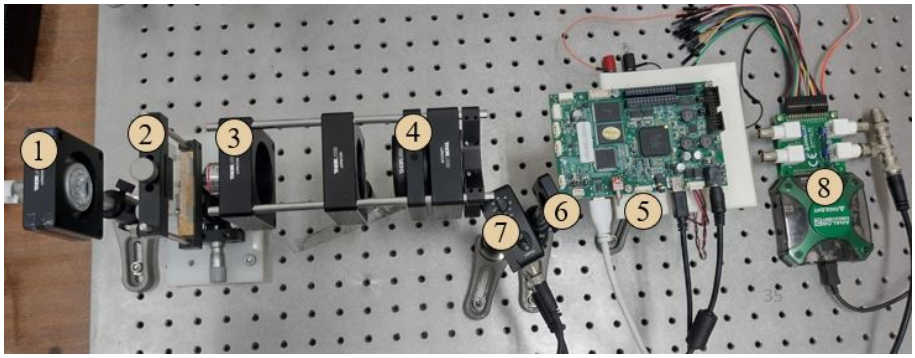

Figure 4.2: Assembly of the SPC viewed from above. 1- Light Source; 2- Target; 3- Objective lens; 4- Tube lens; 5- DLP; 6- Positive lens; 7- Photodiode; 8- DAS.

After the assembly, several calibration tests were carried out so that the microscope was prepared to start the acquisitions and then to evaluate its performance.

Calibrating the microscope was a difficult process as it was not possible to see the light beams with the naked eye. So, an oscilloscope was used to evaluate the amount of light reaching the photodetector. Using this instrument, it was possible to align all the components of the microscope so that it measured the maximum possible intensity. However, even with the use of the oscilloscope, this process was very time-consuming and required some care to get the microscope aligned.

In setting up the microscope there were two configurations available that could be used. The selective light detection configuration was chosen as it was the simplest to set up, align, and focus and required the fewest components.

Using the structured illumination configuration would require the light to pass through the DMD and the objective before reaching the sample. This would substantially reduce the size of the projection patterns which would make the microscope calibration process even more difficult.

4.2 Microscope control process

After the microscope assembly, some control processes were performed as described in section 3.2. Through these processes, it was possible to generate projection images that were subsequently projected onto the DLP. And, in the signal processing, some plots were constructed to extract the final coefficients which were utilised to reconstruct the image.

4.2.1 Generation of the projection images

Therefore, from the developed code of the Hadamard Transform, it was possible to create the images that would be projected on the DLP. Figures 4.3 and 4.4 are examples of these images with 24 Hadamard patterns of 128×128 pixels each. The image in figure 4.3 reflects one of the images created by the MATLAB® code and the image in figure 4.4 presents the negative of that image, i.e. all the patterns of image 4.3 were inverted. The

projection of the inverted image as mentioned in section 3.1, allows the reduction of the SNR of the images resulting from the reconstruction process.

Figure 4.3: Image with 24 Hadamard patterns projected onto the DLP's micro-mirror.

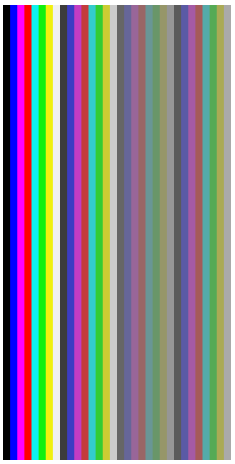

Figure 4.4: Image with 24 inverted Hadamard patterns.

This process was quite fast and allowed to generate patterns with the number of pixels that most easily fitted the images we wanted to obtain. The first generated patterns were of 256×256 pixels, however, the reconstructed images from these patterns with more pixels took much longer to be reconstructed, which delayed the whole process until the final image was obtained.

4.2.2 Signal Processing

To explain the process of the signal processing, the plot of figure 4.5 was constructed. This contains the first 4 images of an acquisition of 1366 images (2 positive and 2 negative). From the data of these 4 images, it was then possible to divide the data into two groups, one of them with the 2 positive images (figure 4.6) and the other with the 2 corresponding negative images (figure 4.7). The red lines presented in figure 4.6 and in figure 4.7 represent

the average of the acquired samples to define a single coefficient for each pattern.

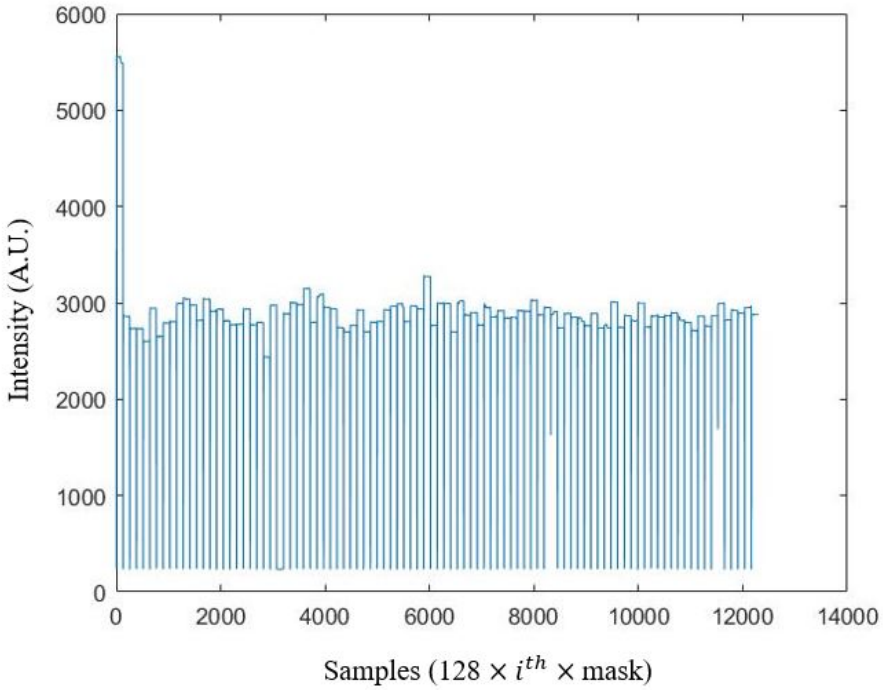

Figure 4.5: Plot of the first 4 images of an acquisition.

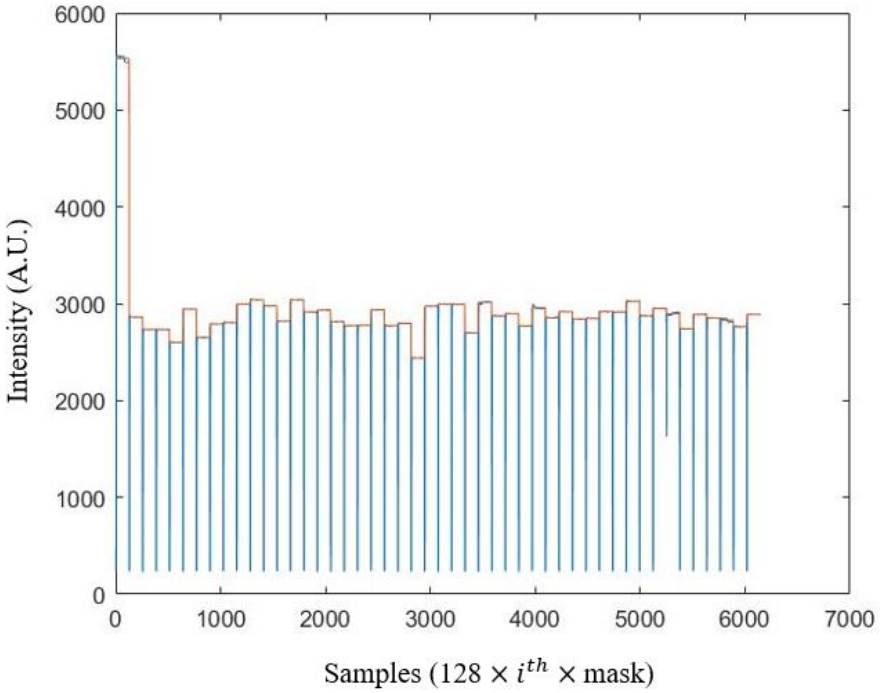

Figure 4.6: Plot of the positive part of the first 4 images of an acquisition.

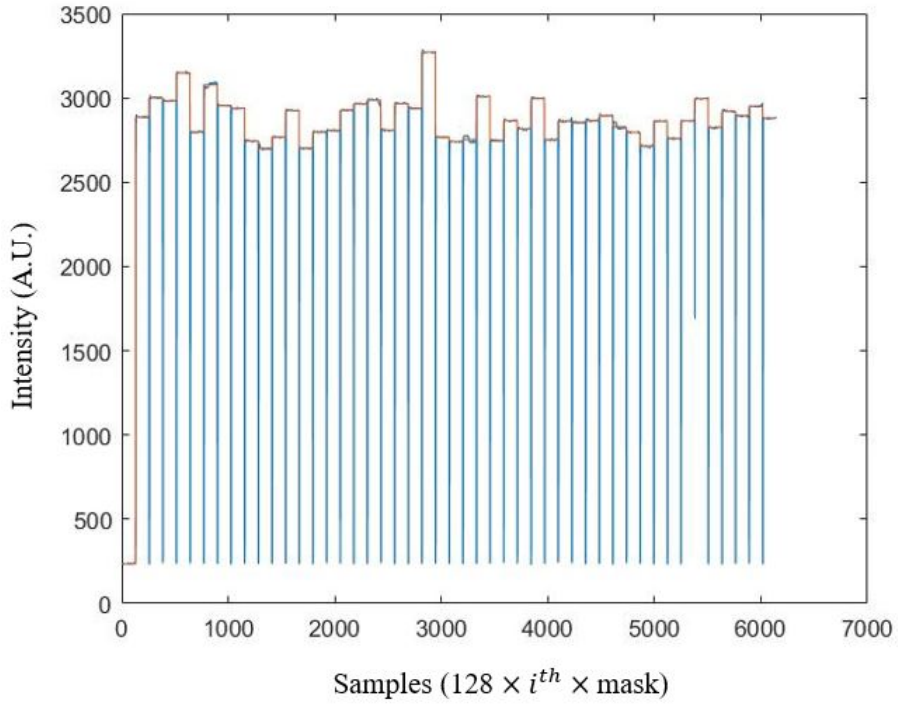

Figure 4.7: Plot of the negative part of the first 4 images of an acquisition.

After dividing the data into two groups, the negative coefficients were subtracted from the positive coefficients to get the final set of coefficients, which were then used to reconstruct the final images, such as those in figures 4.8 (target with millimetre ruler) and 4.9 (1951 USAF resolution test target), using the inverse Hadamard Transform.

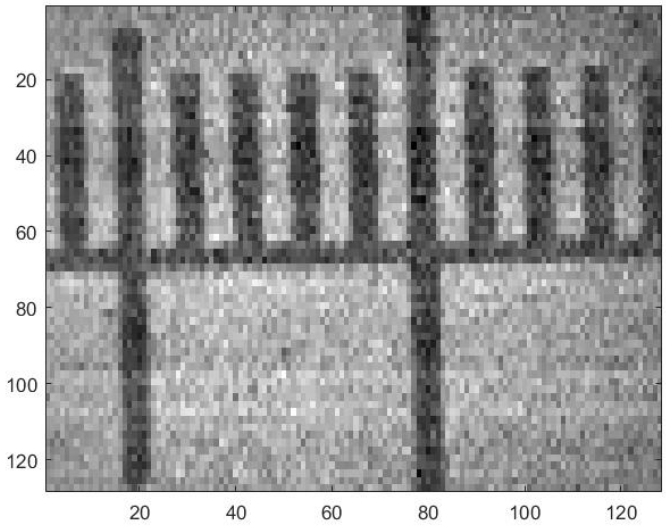

Figure 4.8: Reconstructed image of a target with a millimetre rule with 50% of the coefficients.

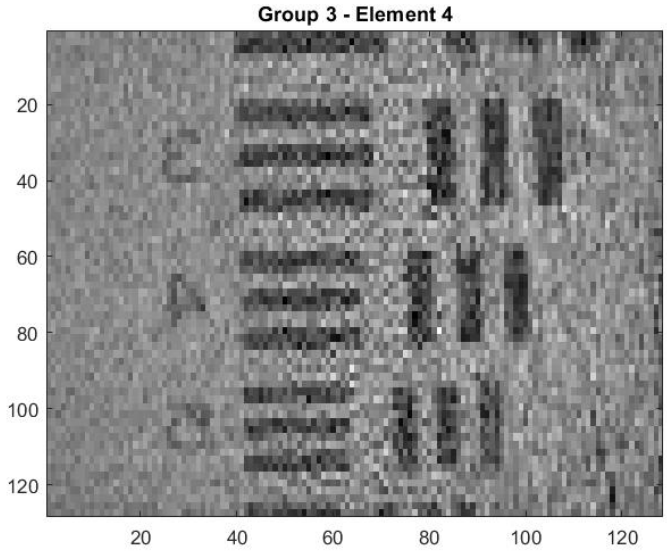

Figure 4.9: Reconstructed image of the third group of the USAF target with 50% of the coefficients.

The whole process of data acquisition and adjustment was a time-consuming procedure, which involved some programming codes so that first the final image coefficients were generated and then the final image was reconstructed.

4.3 Microscope evaluation

After the whole process of assembly and signal processing, the microscope prototype was evaluated for lateral resolution and FOV.

4.3.1 Contrast and Lateral resolution

In order to produce an improved representation of the peaks and valleys of each element of each group acquired, the average of the pixels of the dark zones (vertical and horizontal bars of the USAF 1951 target) and the adjacent light zones between the bars were determined. An example of this process can be seen in figure 4.10.

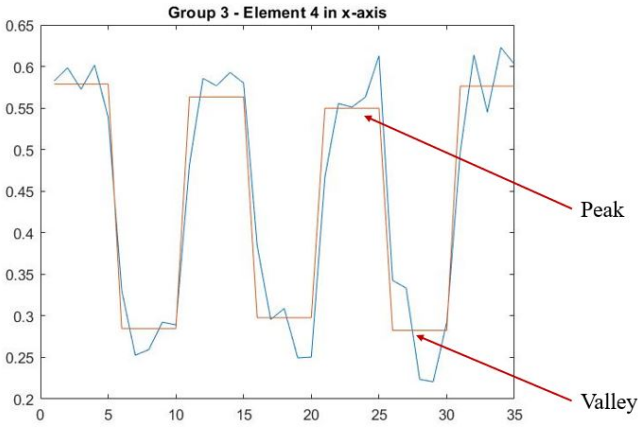

Figure 4.10: Plot of the central line of the USAF lines of element 4 of group 3.

After creating the plots it was then possible to calculate the contrast by subtracting the minimum from the maximum and to choose the elements with the closest contrast of 26.4% for both the x-axis and the y-axis. Group 3 and element 4 were the group and element numbers for the x-axis that were closest to the 26.4% contrast limit, with a contrast of $26.7 \pm 2.3\%$. It was group 3 and element 1 for the y-axis, with a contrast of $28.2 \pm 4.5\%$. Plots of the intensity for both axes are displayed in images 4.10 and 4.11.

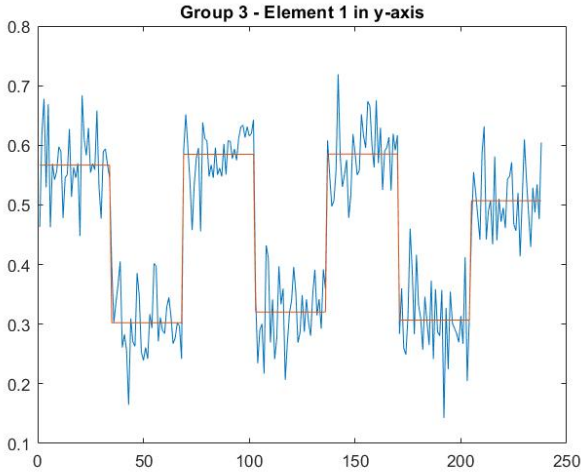

Figure 4.11: Graphic of the final coefficients of element 1 of the group 3 of the USAF 1951 target for the y-axis.

The table 4.1 displays the lateral resolution values related to each group and each element of the USAF target.

Table 4.1: Width of a line in micrometres in USAF Resolving Power Test Target 1951 [47].

	Group Number											
Element	-2	-1	0	1	2	3	4	5	6	7	8	9
1	2000.0	1000.0	500.0	250.0	125.0	62.50	31.25	15.63	7.81	3.91	1.95	0.98
2	1781.80	890.90	445.45	222.72	111.36	55.68	27.84	13.92	6.96	3.48	1.74	0.87
3	1587.40	793.70	396.85	198.73	99.21	49.61	24.80	12.40	6.20	3.10	1.55	0.78
4	1414.21	707.11	353.55	176.78	88.39	44.19	22.10	11.05	5.52	2.76	1.38	0.69
5	1259.92	629.96	314.98	157.49	78.75	39.37	19.69	9.84	4.92	2.46	1.23	0.62
6	1122.46	561.23	280.62	140.31	70.15	35.08	17.54	8.77	4.38	2.19	1.10	0.55

Thus, the lateral resolution values for the x-axis and the y-axis can be seen in the table 4.2.

Table 4.2: Lateral resolution values.

x-axis resolution (μm)	44.19
y-axis resolution (μm)	62.50

Analysing the contrasts obtained in each element and each group it can be concluded that, as theoretically expected, the contrast decreases as the group increases and the element decreases. However, there are some exceptions because the calculated error propagation is very significant for each contrast value.

Comparing the experimental values with the theoretically calculated values in section 3.3.1 it can be concluded that the values are of the same order of magnitude which supports the experimental results. However, as there is a large degree of uncertainty associated with the contrast value, the lateral resolution values also have a large value of uncertainty.

Many acquisitions were made and several contrast values were calculated until the desired contrast values were reached. Some of the images acquired from the various USAF target groups can be analysed in the appendix A.2.

All the images were evaluated with 50% of the coefficients. To evaluate the compressive sensing phenomenon, the images were also reconstructed with a lower percentage of coefficients. Then, 20% of the coefficients and 10% of the coefficients were applied to each element of each acquired group. The 4.12 and 4.13 images show the reconstructed images of element 4 of group 3 with 20% and 10% of the coefficients, respectively. Other examples of this type of image can be analysed in appendix A.3.

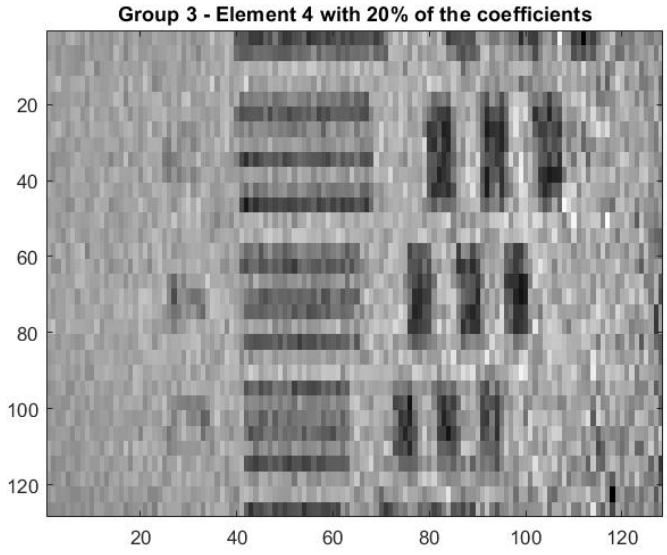

Figure 4.12: Reconstructed image of Group 3 - Element 4 with 20% of the coefficients. Contrast in x-axis= $35.4 \pm 3.4\%$; Contrast in y-axis= $15.8 \pm 3.0\%$.

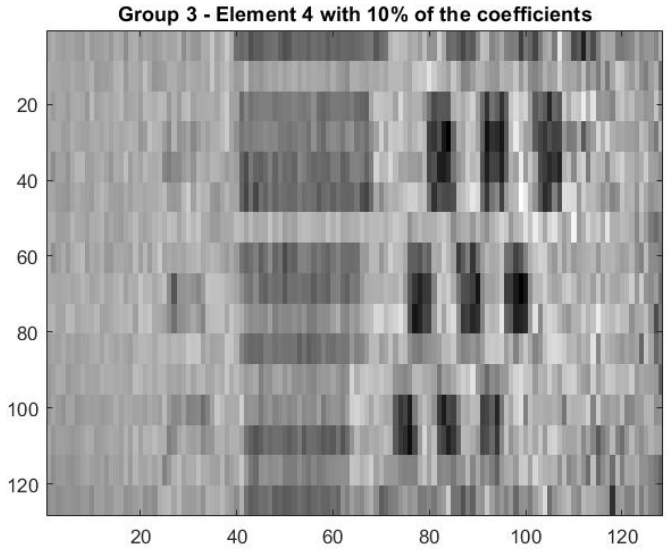

Figure 4.13: Reconstructed image of Group 3 - Element 4 with 10% of the coefficients. Contrast in x-axis= $40.8 \pm 5.3\%$; Contrast in y-axis= $7.2 \pm 2.4\%$.

Regarding the value of the contrast, it can be verified from the example of element 4 of group 3 that as the number of coefficients decreases the contrast in the x-axis increases and the contrast in the y-axis decreases, in general.

Some acquisitions were performed with 100% of the coefficients but there were no relevant changes in the visualization of the images and the contrast values about the acquisitions with 50% of the coefficients.

4.3.2 FOV

The image of the target test produced by the microscope is displayed in Figure 4.14.

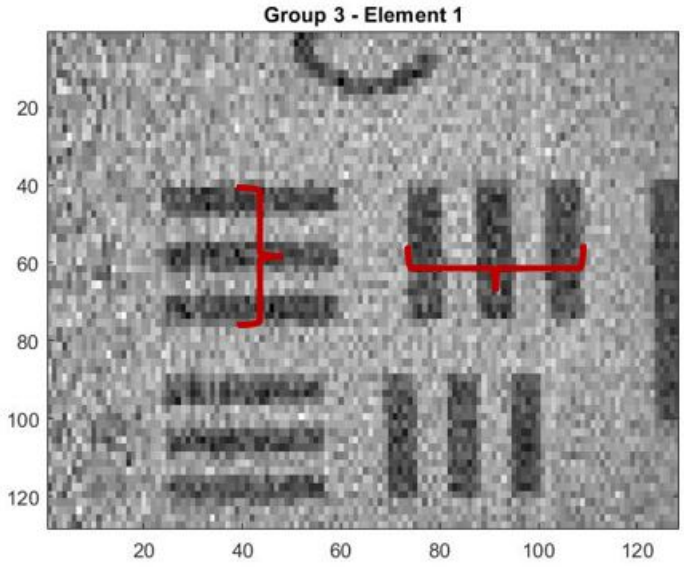

Figure 4.14: Reconstructed image of element 1 of the group 3 of the USAF 1951 target.

The number of pixels between the start point of the first bar and the end point of the last of the three bars was calculated for both the x-axis and the y-axis, as shown in the figure 4.14 by the red curly brackets. The value accounted for was 35 pixels for both axes. From this value and knowing the distance between the bars and the size of the bars (62.5×5), it was possible to calculate the experimental value of FOV.

$$\frac{35pixels}{128pixels} = \frac{312.5\mu m}{FOV}; \tag{4.1}$$

$$FOV = \frac{128 \times 312.5}{35} = 1142.86\mu m. \tag{4.2}$$

With a counting error of 1 pixel for each side of the bar, it was then possible to calculate the error propagation of the FOV value as well.

$$\delta FOV = \frac{128}{35} \times \sqrt{2} = 5.17\mu m. \tag{4.3}$$

Thus, the experimentally measured FOV value was approximately $1.143 \pm 0.005mm$. This value is supported by the next acquired image (figure 4.15), where a millimetre rule measures approximately 1.1 mm from one side of the figure to the other.

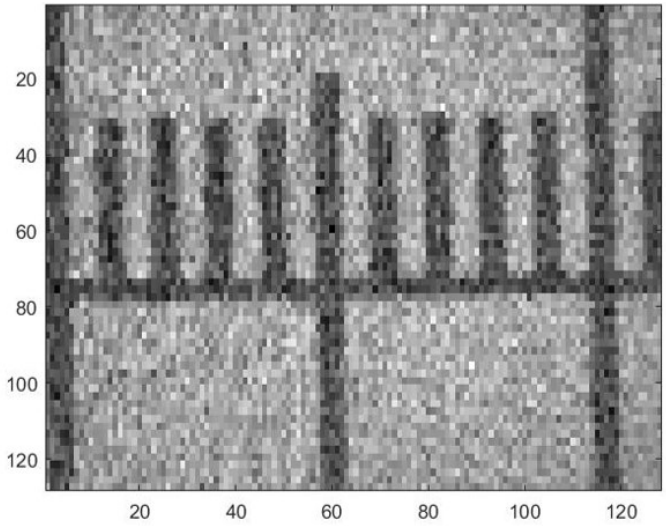

Figure 4.15: Reconstructed image of a millimetre target.

By comparing the theoretical value shown in section 3.3.2 with the experimentally measured value it can be concluded that these are very close which underlines the correct assembly of the microscope.

It should be noted that the microscope's FOV value is relatively high, making it a low magnification device.

4.3.3 Amplification

The experimental amplification value of the single-pixel microscope might be calculated from the FOV value using the following expression:

$$Experimental\ amplification = \frac{DMD\ width}{FOV} = \frac{6.616}{1.14} = 5.80. \tag{4.4}$$

The experimental value of the amplification is very close to the expected value (calculated in section 3.3.3) which also reiterates that the instruments were correctly mounted and aligned.

4.4 Application Case

4.4.1 Imaging through scattering media

In order to test the microscope, imaging through scattering media was elaborated.

Figure 4.16 shows the elaborated assembly for this application. Starting with the LED light source (Fig. 4.16–1), the target (Fig. 4.16–2), a microscope objective (Fig. 4.16–3), and a tube lens (Fig. 4.16–4), the light path was followed. The SPC is then reached, which is made up of a light modulator (Fig. 4.16-5), a sandblasted glass (Fig. 4.16-6), a focusing lens (Fig. 4.16-7), and a photodetector (Fig. 4.16-8) [6].

Figure 4.16: Experimental-set up [6]. 1- Light Source; 2- Target; 3- Objective lens; 4- Tube lens; 5- DLP; 6- Sandblasted glass; 7- Positive lens; 8- Photodiode.

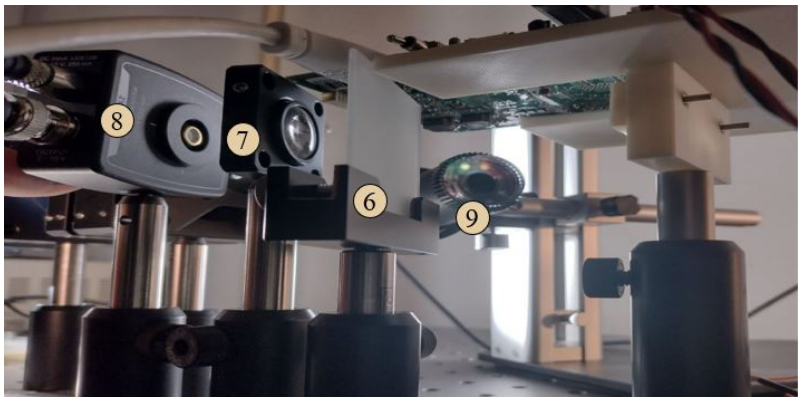

Figure 4.17: Close-up photograph of the experimental set-up [6]. 6- Sandblasted glass; 7- Positive lens; 8- Photodiode; 9- CCD Camera.

Figure 4.17 displays a close-up image of the sandblasted glass. The same image also displays the CCD camera (fig. 4.17–9) that was used to capture the target's microscopic image for comparison [6].

Using this setup, four different experimental outcomes were achieved. With and without the sandblasted glass, the USAF target was photographed twice with the SPC and once with a Conventional Imaging System (CIS).

The microscope setup projected the USAF group 2 element 5 into the light modulator.

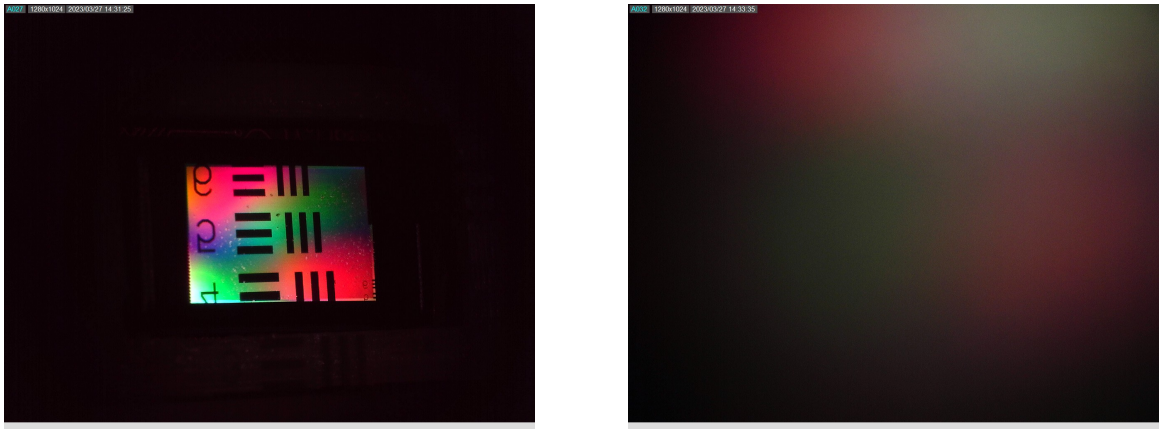

(a) CIS. (b) CIS scattering media.

Figure 4.18: USAF target images acquired using the Conventional Imaging System (CIS) with and without the scattering medium.

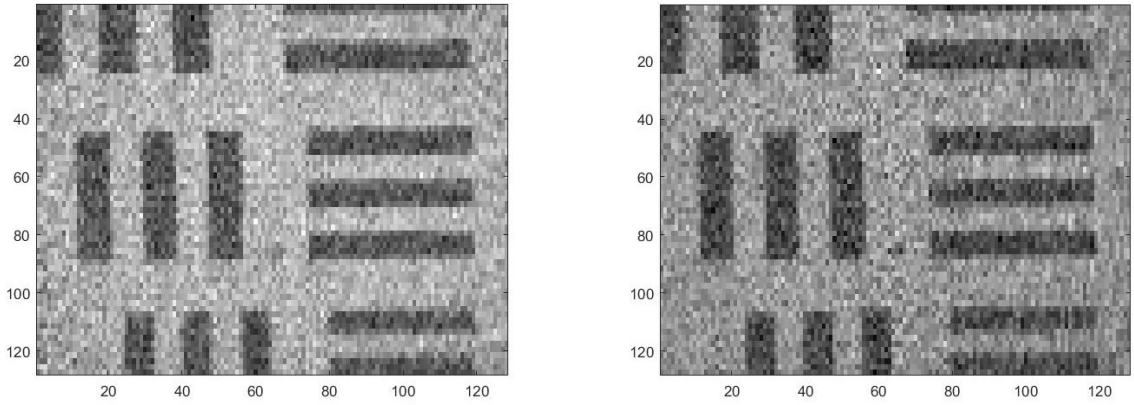

(a) SPC. (b) SPC scattering media.

Figure 4.19: USAF target images acquired using the SPC with and without the scattering medium.

By aligning all of the DMD's mirrors in the same direction, the CIS was able to capture a picture of the target in the light modulator plane (fig. 4.18a). The target is clearly visible in this shot, and it is simple to distinguish the USAF's vertical and horizontal lines. In contrast, the light wavefront is entirely scrambled when the sandblasted glass is positioned between the CIS and the light modulator, making it impossible to determine the target's structure (fig. 4.18b). When using a CIS, the impact of the scattering medium addition is crucial [6].

The SPC was also used to photograph the same target under the same circumstances. The SPC picture from Figure 4.19a is shown without the glass that has been sandblasted. When compared to the image from the traditional imaging method, the SPC image exhibits a horizontal and vertical flip. Although there are only 128×128 pixels in the image, the clarity of the reconstructed image still makes it possible to distinguish between the

horizontal and vertical lines. The reconstructed image with the sandblasted glass is shown in Figure 4.19b. When compared to the impact it has on the standard imaging system, the influence of inserting the sandblasted glass is greatly diminished. In this particular case, the horizontal lines of the target provide evidence of only a slight loss in image contrast and an increase in noise [6].

The primary limitation of this experiment is that it uses a simplified representation of a real case. In this study, we took into account the possibility of a scattering medium only after the light modulator in both the simulation and experimental studies. As a result, a clear light wavefront is produced up to the light modulator, which can then execute structured segmentation on a target image that is also clearly visible. The SPC arrangement makes this problem easier to handle because the scattering medium does not show until after the light has been modified [6].

When the light reaches the light modulator in a practical situation, the target will be embedded in the scattering medium, resulting in a scrambled wavefront. The intensity modulation is then applied to a wavefront that has already lost spatial coherence and has been scrambled. This fact creates issues in this configuration because other target zones have already contributed to the areas chosen by the DMD. A configuration based on structured illumination may perform better in this case [6].

This application demonstrated how a single-pixel camera performs better than a traditional pixelated imaging system when a scattering medium is positioned in front of the subject. The experimental setup also demonstrated that a microscope SPC can reconstruct images from a USAF target with comparable quality whether or not the target is obscured by sandblasted glass [6].

5

Conclusions

In this thesis, a microscopy-based single-pixel camera setup was created to carry out intensity imaging using compressive sensing principles.

The overall results presented in this project indicate that the elaborated microscope was able to evaluate the intended targets successfully. However, this assembly presented some limitations such as for each change or displacement of the target, there is the possibility of misalignment and consequent blurring of the microscope, which leads to some defects in the quality of the final reconstructed image and time-consuming realignment processes. Another limitation is related to the luminosity of the place where the acquisitions were made since, although they were made in a dark room, some ambient light may have interfered with the final images causing some noise.

The experimental value of FOV is close to the theoretically calculated value so it can be concluded that the microscope set-up was done correctly and that the intended objective was reached.

The value of lateral resolution for the x-axis was 44.19 μm, which represents a value above the requirement defined earlier in chapter 1. The value of the lateral resolution was 62.50 μm for the y-axis, which, like the value of the lateral resolution in the x-axis, represents a value of the same order of magnitude as the defined requirement but slightly above the desired one. This is due to the fact that a low magnification objective lens was used, 4$\times$ more specifically.

In order to decrease these resolution values to get closer to the values defined in the requirements, an image with more pixels, for example, 256×256, could be tested or an objective lens with more magnification could be used.

The experimental FOV value was 1.143 ± 0.005 mm. This value is of the same order of magnitude and quite close to the value defined for this characteristic in the requirements section of chapter 1, concluding that this requirement was fulfilled. To bring this value even closer to the requirement value, a DMD with a larger area could be used.

It should be noted that by using a lens with more magnification, the lateral resolution would decrease, as intended, but the FOV would also decrease, which is not intended. To improve these two characteristics, a higher magnification lens and a DMD with a larger area could be used at the same time.

Regarding the application case, when a scattering medium is placed in front of the

subject, a single-pixel camera outperforms a conventional pixelated imaging system, i.e. this application case was a success as whether or not sandblasted glass obscures a USAF target, a microscope SPC can recreate images from the target with identical fidelity.

5.1 Future work

Some adjustments to the SPC design are required to improve these results. For example, the use of a lateral illumination (placing the light source at 90° directed to a dichroic mirror placed between the objective and the tube lens) combined with the use of a reflection microscope could be a solution to increase the amount of light reaching the DMD and subsequently the photodiode. With this type of illumination, the acquisition of images with fluorescent substances could be facilitated.

Another point for future work will be to increase the magnification of the microscope, changing the 4× objective to a 10× objective, for example.

Also, fluorescent microspheres may be used for PSF calculation. Thus, it will be possible to observe the point like sources with more definition and consequently determine the PSF.

The implementation of more advanced image reconstruction techniques, including TVAL3, deep learning (neural networks), and plug-and-play algorithms, could be another topic to improve. These methods outperform the basic linear combination of measurements, but they require the solution of lengthy optimization problems or training on big data sets, both of which come with substantial computing costs.

The application of the microscope to the field of biomedicine would also be something to work on. Using biological samples as this type of microscope could help in the diagnosis of various mutations at the cellular level in a faster and less expensive way compared to the devices currently in use.

Bibliography

[1] C. Shannon, "Communication in the presence of noise," *Proceedings of the IRE*, vol. 37, no. 1, pp. 10–21, 1949.

[2] M. F. Duarte, M. A. Davenport, D. Takhar, J. N. Laska, T. Sun, K. F. Kelly, and R. G. Baraniuk, "Single-pixel imaging via compressive sampling," *IEEE Signal Processing Magazine*, vol. 25, no. 2, pp. 83–91, 2008.

[3] L. Ordóñez, E. Ipus, A. J. Lenz, J. Lancis, and E. Tajahuerce, "Optical sectioning microscopy with structured illumination and single-pixel detection," in *Three-Dimensional and Multidimensional Microscopy: Image Acquisition and Processing XXX*, vol. 12385, pp. 7–9, SPIE, 2023.

[4] P. P. d. Santos *et al.*, "Phosphorescence lifetime imaging of o2 sensitive biomarkers using a single pixel detector," Master's thesis, 2021.

[5] M. P. Edgar, G. M. Gibson, and M. J. Padgett, "Principles and prospects for single-pixel imaging," 1 2019.

[6] P. Vaz, B. Guerra, and J. Cardoso, "Single-pixel imaging: concepts and application to imaging through scattering media.," in *International Conference on Transparent Optical Networks*, IEEE, 2023.

[7] P. G. Vaz, A. S. Gaudêncio, L. F. R. Ferreira, A. Humeau-Heurtier, M. Morgado, and J. Cardoso, "Re-ordering of hadamard matrix using fourier transform and gray-level co-occurrence matrix for compressive single-pixel imaging in low resolution images," *IEEE Access*, vol. 10, pp. 46975–46985, 2022.

[8] P. Sen, B. Chen, G. Garg, S. R. Marschner, M. Horowitz, M. Levoy, and H. P. Lensch, "Dual photography," in *ACM SIGGRAPH 2005 Papers*, pp. 745–755, 2005.

[9] G. M. Gibson, S. D. Johnson, and M. J. Padgett, "Single-pixel imaging 12 years on: a review," *Opt. Express*, vol. 28, pp. 28190–28208, Sep 2020.

[10] M. F. Duarte, M. A. Davenport, D. Takhar, J. N. Laska, T. Sun, K. F. Kelly, and R. G. Baraniuk, "Single-pixel imaging via compressive sampling," *IEEE signal processing magazine*, vol. 25, no. 2, pp. 83–91, 2008.

[11] M. F. Duarte, M. A. Davenport, D. Takhar, J. N. Laska, T. Sun, K. F. Kelly, and R. G. Baraniuk, "Single-pixel imaging via compressive sampling," *IEEE Signal Processing Magazine*, vol. 25, no. 2, pp. 83–91, 2008.

[12] J. Romberg, "Imaging via compressive sampling," *IEEE Signal Processing Magazine*,

vol. 25, no. 2, pp. 14–20, 2008.

[13] P. G. Vaz, D. Amaral, L. F. R. Ferreira, M. Morgado, and J. ao Cardoso, "Image quality of compressive single-pixel imaging using different hadamard orderings," *Opt. Express*, vol. 28, pp. 11666–11681, Apr 2020.

[14] K. J. Horadam, *Hadamard Matrices and Their Applications*. Princeton University Press, 2007.

[15] C. Zhuoran, Z. Honglin, J. Min, W. Gang, and S. Jingshi, "An improved hadamard measurement matrix based on walsh code for compressive sensing," in *2013 9th International Conference on Information, Communications Signal Processing*, pp. 1–4, 2013.

[16] C. Li, "An efficient algorithm for total variation regularization with applications to the single pixel camera and compressive sensing," 01 2011.

[17] I. Hoshi, T. Shimobaba, T. Kakue, and T. Ito, "Single-pixel imaging using a recurrent neural network combined with convolutional layers," *Opt. Express*, vol. 28, pp. 34069–34078, Nov 2020.

[18] Y. Tian, Y. Fu, and J. Zhang, "Plug-and-play algorithms for single-pixel imaging," *Optics and Lasers in Engineering*, vol. 154, p. 106970, 2022.

[19] T. U. of Edinburgh, "What is microscopy?," Sep 2018.

[20] S. Museum, "The microscope.," Aug 2019.

[21] B. R. Masters, "History of the optical microscope in cell biology and medicine," *eLS*, 2008.

[22] M. W. Davidson and M. Abramowitz, "Optical microscopy," *Encyclopedia of imaging science and technology*, vol. 2, no. 1106-1141, p. 120, 2002.

[23] M. Abramowitz and M. W. Davidson, "Optical microscopy primer - anatomy of the microscope.," Sep 2018.

[24] N. Instruments, "Microscopyu - the source for microscopy education," 2023.

[25] M. Saxena, G. Eluru, and S. S. Gorthi, "Structured illumination microscopy," *Adv. Opt. Photon.*, vol. 7, pp. 241–275, Jun 2015.

[26] J. Huisken and D. Y. R. Stainier, "Selective plane illumination microscopy techniques in developmental biology," *Development*, vol. 136, pp. 1963–1975, 06 2009.

[27] H. I. Academy, "Scientific volume imaging - point spread function."

[28] B. Sun, M. P. Edgar, R. Bowman, L. E. Vittert, S. Welsh, A. Bowman, and M. J. Padgett, "3d computational imaging with single-pixel detectors," *Science*, vol. 340, pp. 844–847, 5 2013.

[29] F. Magalhães, "High-resolution hyperspectral single-pixel imaging system based on compressive sensing," *Optical Engineering*, vol. 51, p. 071406, 5 2012.

[30] S. Jiao, J. Feng, Y. Gao, T. Lei, Z. Xie, and X. Yuan, "Optical machine learning with incoherent light and a single-pixel detector," *Opt. Lett.*, vol. 44, pp. 5186–5189, Nov 2019.

[31] J. Greenberg, K. Krishnamurthy, and D. Brady, "Compressive single-pixel snapshot x-ray diffraction imaging," *Optics Letters*, vol. 39, p. 111, 1 2014.

[32] P. Santos, P. G. Vaz, A. S. Gaudêncio, M. Morgado, N. A. M. Pereira, M. Pineiro, T. M. P. e Melo, and J. Cardoso, "Compressive single pixel phosphorescence lifetime and intensity simultaneous imaging: a pilot study using oxygen sensitive biomarkers," p. 33, SPIE-Intl Soc Optical Eng, 4 2021.

[33] N. Radwell, K. J. Mitchell, G. M. Gibson, M. P. Edgar, R. Bowman, and M. J. Padgett, "Single-pixel infrared and visible microscope," *Optica*, vol. 1, p. 285, 11 2014.

[34] A. Y. Yuan, J. Feng, S. Jiao, Y. Gao, Z. Zhang, Z. Xie, L. Du, and T. Lei, "Adaptive and dynamic ordering of illumination patterns with an image dictionary in single-pixel imaging," *Optics Communications*, vol. 481, 2 2021.

[35] S. Grönroos, W. Lund, and J. Björkqvist, "A single pixel camera based on a dlp video projector."

[36] A. D. Rodríguez, P. Clemente, E. Tajahuerce, and J. Lancis, "Dual-mode optical microscope based on single-pixel imaging," *Optics and Lasers in Engineering*, vol. 82, pp. 87–94, 7 2016.

[37] Y. Liu, J. Suo, Y. Zhang, and Q. Dai, "Single-pixel phase and fluorescence microscope," *Optics Express*, vol. 26, p. 32451, 12 2018.

[38] M. Yao, Z. Cai, X. Qiu, S. Li, J. Peng, and J. Zhong, "Full-color light-field microscopy via single-pixel imaging," *Optics Express*, vol. 28, p. 6521, 3 2020.

[39] J. Peng, M. Yao, Z. Huang, and J. Zhong, "Fourier microscopy based on single-pixel imaging for multi-mode dynamic observations of samples," *APL Photonics*, vol. 6, p. 046102, 4 2021.

[40] H. Deng, G. Wang, Q. Li, Q. Sun, M. Ma, and X. Zhong, "Transmissive single-pixel microscopic imaging through scattering media," *Sensors*, vol. 21, 4 2021.

[41] T. Instruments., "Ti dlp® lightcrafter™ 4500 evaluation module user's guide.," Jul 2017.

[42] Digilent., "Analog discovery 2™ reference manual.," Sep 2015.

[43] Thorlabs., "Pda36a2 si switchable gain detector user guide.," Apr 2020.

[44] E. Optics., "Olympus pln 4x objective.," Apr 2023.

[45] Z. Zhang, X. Wang, G. Zheng, and J. Zhong, "Hadamard single-pixel imaging versus fourier single-pixel imaging," *Opt. Express*, vol. 25, pp. 19619–19639, Aug 2017.

[46] R. N. Hotchkiss, F. E. Washer, and F. W. Rosberry, "Spurious resolution of photographic lenses∗," *J. Opt. Soc. Am.*, vol. 41, pp. 600–603, Sep 1951.

[47] Wikipedia., "1951 usaf resolution test chart.," Jul 2022.

[48] K. R. Spring, T. J. Fellers, and M. W. Davidson., "Resolution and contrast in confocal microscopy.."

Appendices

A

Supplementary data

A.1 Generation of the projection images

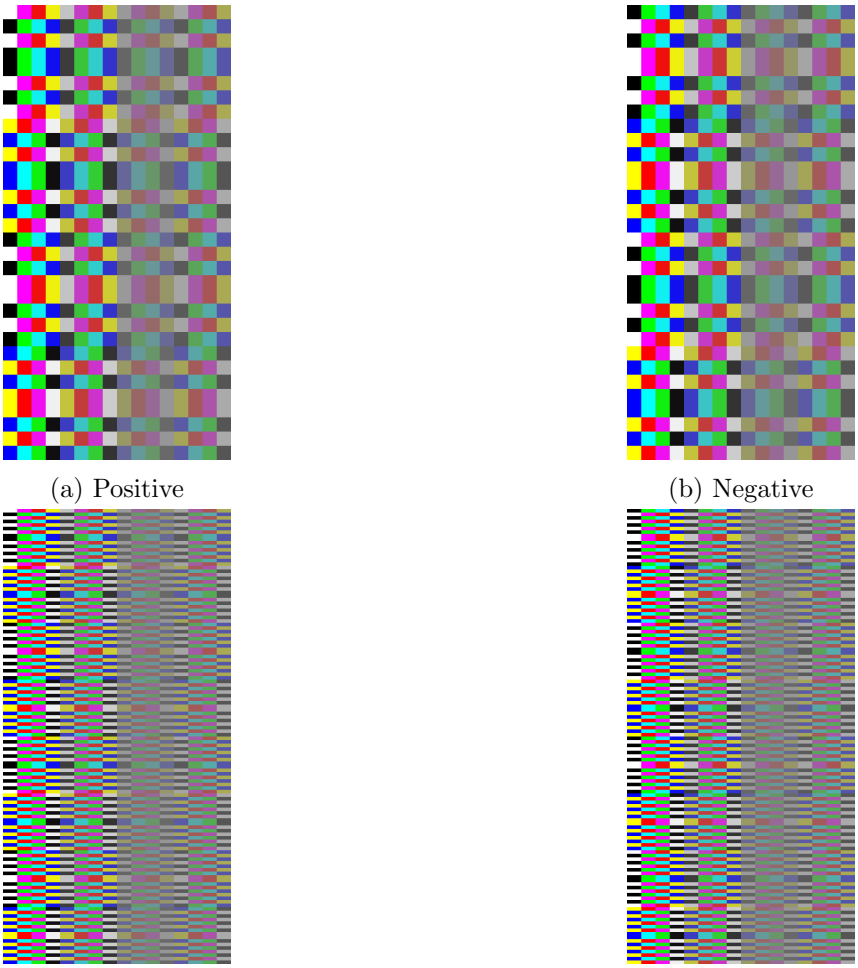

(a) Positive (b) Negative

(c) Positive (d) Negative

Figure A.1: Examples of images with 24 Hadamard patterns projected into the DLP's micro-mirror.

A.2 Reconstructed images and contrast calculation

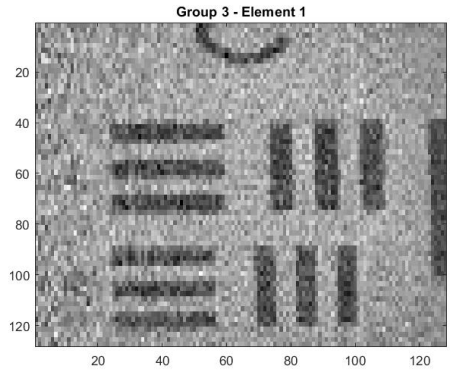

(a) Group 3 - Element 1. Contrast in x-axis= 36.6±2.1%; Contrast in y-axis= 28.2± 4.5%.

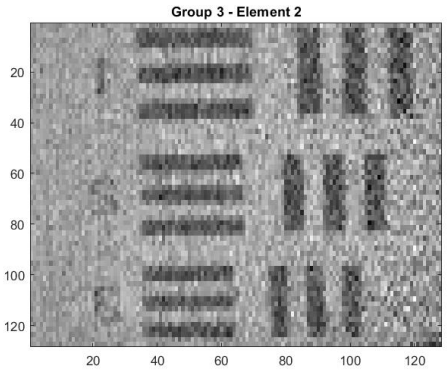

(b) Group 3 - Element 2. Contrast in x-axis= 33.4±0.8%; Contrast in y-axis= 26.3± 2.7%.

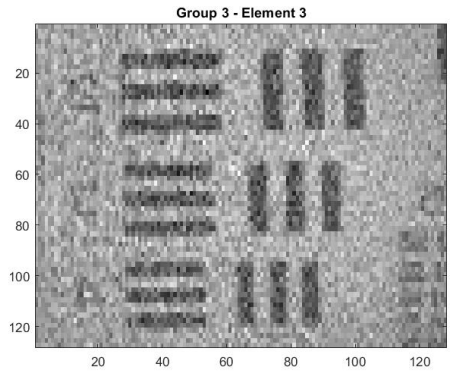

(c) Group 3 - Element 3. Contrast in x-axis= 27.9±2.4%; Contrast in y-axis= 25.0±6.1%.

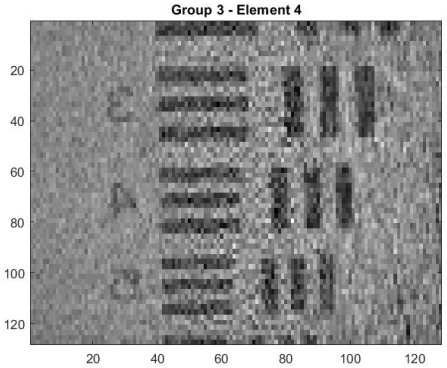

(d) Group 3 - Element 4. Contrast in x-axis= 26.7±2.3%; Contrast in y-axis= 24.2± 7.8%.

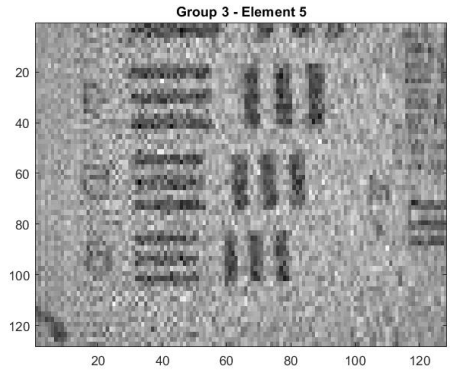

(e) Group 3 - Element 5. Contrast in x-axis= 25.8±4.1%; Contrast in y-axis= 19.6±8.5%.

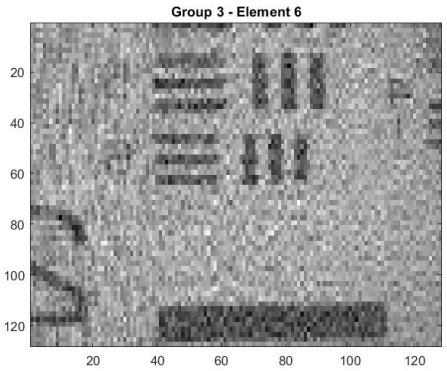

(f) Group 3 - Element 6. Contrast in x-axis= 24.3±3.0%; Contrast in y-axis= 19.1±7.1%.

Figure A.2: Reconstructed images of Group 3 with 50% of the coefficients.

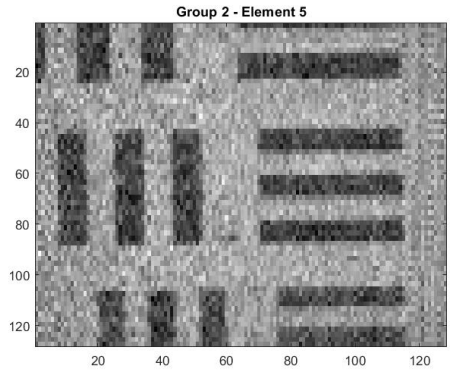

(a) Group 2 - Element 5. Contrast in x-axis= 32.6±2.8%; Contrast in y-axis= 35.2± 4.7%.

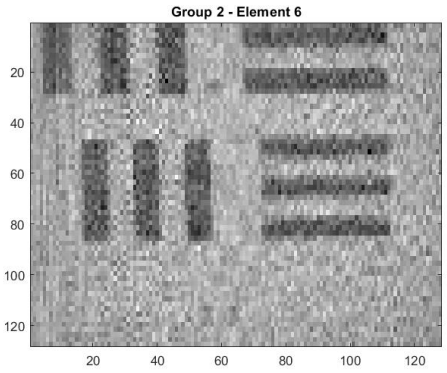

(b) Group 2 - Element 6. Contrast in x-axis= 28.4±2.6%; Contrast in y-axis= 25.6± 4.9%.

Figure A.3: Reconstructed images of Group 2 with 50% of the coefficients.

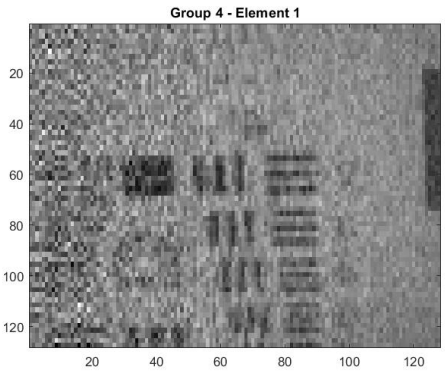

(a) Group 4 - Element 1. Contrast in x-axis= 16.1±4.5%; Contrast in y-axis= 15.4± 3.2%.

Figure A.4: Reconstructed image of Group 4 with 50% of the coefficients.

A.3 Reconstructed images with less number of coefficients

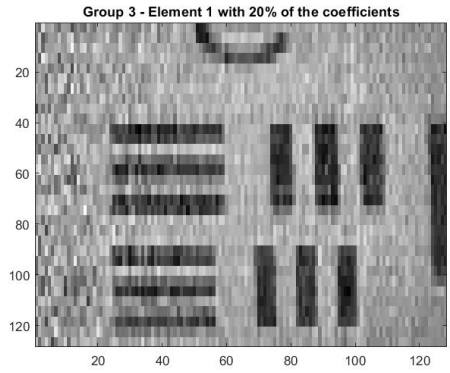

(a) With 20% of the coefficients. Contrast in x-axis= $50.7 \pm 3.4\%$; Contrast in y-axis= $32.2 \pm 5.8\%$.

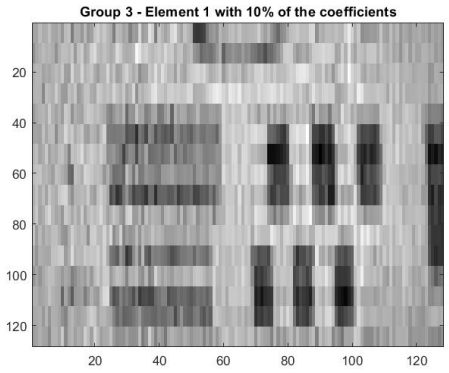

(b) With 10% of the coefficients. Contrast in x-axis= $54.8 \pm 2.4\%$; Contrast in y-axis= $5.2 \pm 3.4\%$.

Figure A.5: Reconstructed images of Group 3 - Element 1.

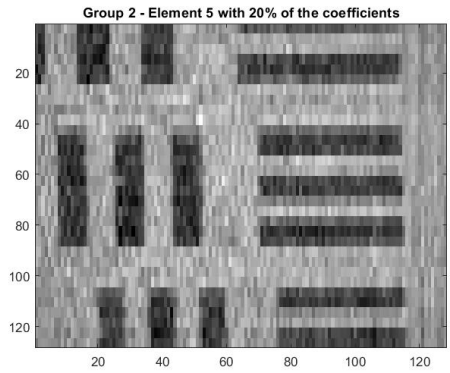

(a) With 20% of the coefficients. Contrast in x-axis= $38.9 \pm 4.0\%$; Contrast in y-axis= $31.4 \pm 3.7\%$.

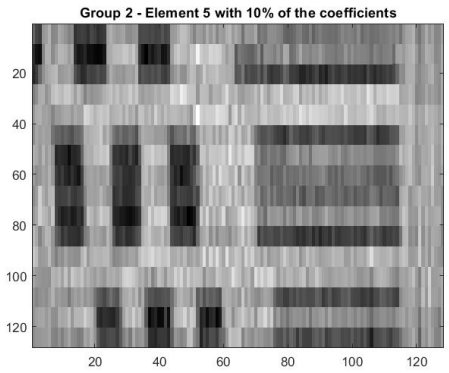

(b) With 10% of the coefficients. Contrast in x-axis= $43.0 \pm 2.4\%$; Contrast in y-axis= $16.5 \pm 4.2\%$.

Figure A.6: Reconstructed images of Group 2 - Element 5.

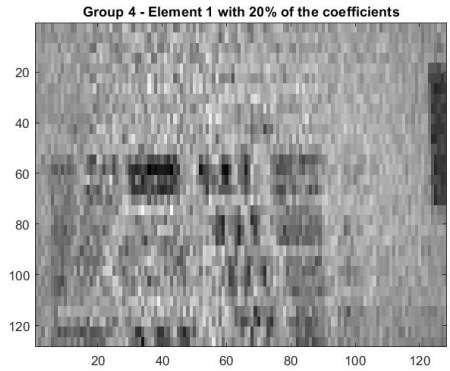

(a) With 20% of the coefficients. Contrast in x-axis= $22.1 \pm 6.0\%$; Contrast in y-axis= $3.2 \pm 3.1\%$.

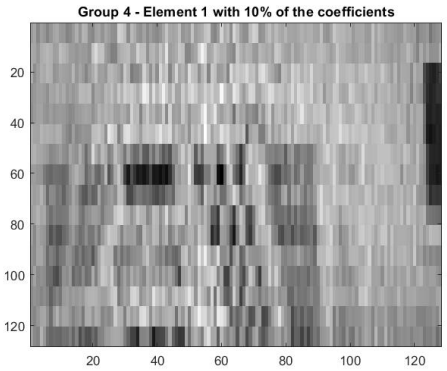

(b) With 10% of the coefficients. Contrast in x-axis= $25.7 \pm 7.4\%$; Contrast in y-axis= $0.0 \pm 3.6\%$.

Figure A.7: Reconstructed images of Group 4 - Element 1.